Journal of Nanobiotechnology

RESEARCH

Open Access

Single-cell multi-omics analysis reveals the mechanism of action of a novel antioxidant polyphenol nanoparticle loaded with STAT3 agonist in mediating cardiomyocyte ferroptosis to ameliorate age-related heart failure

Haoyuan Zheng[1], Yuan Tian[2], Dongyu Li[1] and Yanxiao Liang[1*]

Abstract

Background Heart failure (HF) is a prevalent and critical cardiac condition that leads to profound structural and functional changes in the heart. Although traditional treatments have shown partial efficacy, the long-term outcomes remain suboptimal. Emerging research has highlighted the pivotal role of oxidative stress and ferroptosis in HF progression. This study investigates a new therapeutic approach utilizing antioxidant polyphenol nanoparticles loaded with a STAT3 agonist (PN@Col) to target these pathways and improve age-related HF.

Results Key cells and genes contributing to HF progression were identified via analysis of the GEO database, with single-cell RNA sequencing (scRNA-seq) and AUCell analysis used to evaluate differential gene expression. The STAT3 gene was highlighted as essential, and its functionality was further validated in vitro through cell experiments, confirming its impact on cardiomyocytes (CMs) in HF. Following the development of PN@Col, in vitro experiments showed that PN@Col effectively reduced oxidative stress and ferroptosis in CMs. In vivo studies in elderly HF mice demonstrated significant improvements in cardiac function following PN@Col treatment.

Conclusions PN@Col offers a promising therapeutic approach to age-related HF by mitigating oxidative stress and ferroptosis in cardiomyocytes. These findings provide a solid scientific foundation for PN@Col as a potential novel treatment strategy for HF, supporting further exploration toward clinical application.

Keywords Heart failure, Oxidative stress, Ferroptosis, Signal transducer and activator of transcription 3, Polyphenol nanoparticles

*Correspondence:
Yanxiao Liang
liangyx_cmu@126.com
Full list of author information is available at the end of the article

Graphical Abstract

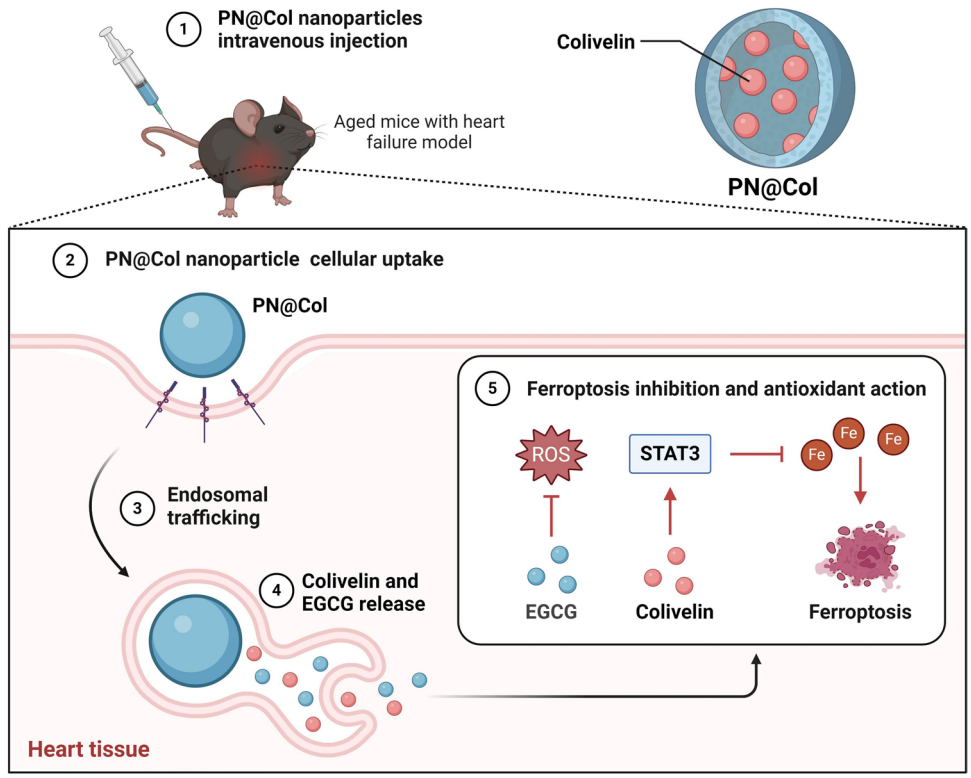

Introduction

Heart failure (HF) is a serious and common cardiovascular disease characterized by the heart's inability to effectively pump enough blood to meet the body's needs [1, 2]. This condition significantly reduces patients' quality of life and markedly increases mortality rates [3, 4]. Globally, the incidence and prevalence of HF have been steadily increasing, imposing a heavy burden on public health [5]. Current clinical management of HF primarily relies on pharmacological treatments such as beta-blockers, angiotensin-converting enzyme (ACE) inhibitors, and angiotensin II receptor blockers (ARBs), which alleviate symptoms by easing cardiac workload and improving circulation [6, 7]. Additionally, mechanical support devices like ventricular assist devices (VADs) and cardiac resynchronization therapy (CRT), along with eventual heart transplant surgery, are available [8, 9]. While these interventions can offer short-term symptom relief and improve quality of life, the long-term prognosis remains suboptimal, leading many patients to eventually necessitate heart transplants [10, 11]. Therefore, there is an urgent need to develop new therapeutic strategies aimed at enhancing the long-term prognosis and quality of life for individuals with HF.

In recent years, an increasing body of research indicates that oxidative stress plays a crucial role in the pathophysiological processes of HF [12, 13]. Oxidative stress refers to the imbalance between the generation and clearance of free radicals and reactive oxygen species (ROS) in the body, resulting in cellular and tissue damage [14, 15]. Elevated levels of ROS not only directly harm cardiomyocytes (CMs) but also exacerbate the progression of HF by triggering inflammatory responses and various cell death pathways such as apoptosis and ferroptosis [16, 17]. Ferroptosis is a novel programmed cell death mechanism characterized by intracellular iron overload and lipid peroxidation reactions [18, 19]. In HF, the occurrence of ferroptosis significantly damages CMs, making targeted therapies against oxidative stress and ferroptosis, such as antioxidants and iron chelators, a prominent focus in HF research [19, 20]. Nevertheless, the effective delivery of these therapeutic molecules and maximizing their efficacy remain significant challenges in current research efforts.

Polyphenols are a category of natural compounds with potent antioxidant activity, widely present in fruits, vegetables, and tea [21]. These compounds not only directly scavenge free radicals and reduce oxidative stress but also exert protective effects by modulating various cellular signaling pathways [21]. In recent years, with the advancement of nanotechnology, polyphenol nanoparticles (PNs) have emerged as a novel drug delivery system [22, 23]. Unlike fully synthetic nanoparticles, these polyphenol nanoparticles have higher bioavailability and targeting ability, allowing them to stably exist in vivo, effectively deliver drugs to specific lesion sites, and be enzymatically degraded, dissolved, or broken down into non-toxic small molecules or metabolites through physicochemical actions [24, 25]. Furthermore, loading therapeutic molecules onto PNs can further enhance their therapeutic effects. For example, utilizing PNs to deliver antioxidants and ferroptosis regulators can not only improve drug stability and bioavailability but also effectively synergize to suppress oxidative stress and ferroptosis, thereby alleviating the progression of HF [22, 26]. Consequently, employing PNs for therapeutic molecule delivery holds promise as an effective strategy for treating HF.

Signal transducer and activator of transcription 3 (STAT3) is a crucial transcription factor involved in regulating various cellular processes, including cell proliferation, differentiation, apoptosis, and immune responses [27, 28]. Recent studies have revealed the significant role of STAT3 in the occurrence and progression of HF [29, 30]. Specifically, STAT3 plays a critical role in CMs' biological functions by regulating ferroptosis and inflammatory responses [31, 32]. For instance, activation of STAT3 can decrease ferroptosis, protect CMs, and thereby improve the prognosis of HF [33]. Consequently, targeted modulation of STAT3 activity holds promise as a novel therapeutic strategy for treating HF. This study innovatively proposes the use of a novel antioxidant PN loaded with a STAT3 agonist (PN@Col) as a new therapeutic approach for age-related HF. We systematically evaluated the effectiveness of this strategy through in vitro cell experiments and in vivo mouse models, investigating its potential mechanisms of action.

This study aimed to explore the therapeutic effects of PN@Col in improving age-related HF by modulating CM ferroptosis. Specifically, we initially identified key cell types and genes crucial in the progression of HF through single-cell RNA sequencing (scRNA-seq) analysis. Subsequently, we validated the essential role of STAT3 in regulating CM ferroptosis through in vitro cell experiments and prepared PN@Col. Through both in vitro and in vivo experiments, we assessed the impact of PN@Col on the biological functions of CMs and ferroptosis, investigating its therapeutic effects in an age-related HF mouse model. The results of the study demonstrated that PN@Col significantly suppressed CM ferroptosis, improved cellular biological functions, and notably enhanced heart function in aged HF mice. This discovery provides new insights and strategies for the treatment of age-related HF, holding significant scientific and clinical implications. Through this research, we have provided scientific evidence and theoretical support for enhancing the prognosis of age-related HF patients clinically, promoting the application and advancement of antioxidant PNs in cardiac disease treatment.

Results and discussion

Cellular heterogeneity and cell type analysis in human heart tissue of HF

To investigate the impact of cellular heterogeneity in heart tissue of HF patients, we analyzed scRNA-seq data from the GEO database. After data quality control cells with fewer than 2,000 expressed genes (UMI) were filtered out (Fig. S1A), and cells with mitochondrial expression < 5% or ribosomal gene expression > 20% were retained. Statistical analysis was performed using perCellQCMetrics (Fig. S1B-C). Linear scaling (ScaleData) and PCA (RunPCA) identified the first two PCs (Fig. S1D), followed by a heatmap of gene expression profiles for PC_1 to PC_7 (Fig. S1E) and cell distribution visualization (Fig. S1F). RunHarmony was applied to reduce batch effects, improving clustering accuracy (Fig. S1G–I).

Subsequently, we employed the UMAP algorithm to perform non-linear dimensionality reduction on the first 7 PCs, clustering all cells into 30 cell clusters (Fig. S2A). The distribution of cells within each cell cluster is depicted in Fig. S2B-C, while the proportion of cell numbers in each cell cluster is illustrated in Fig. S2D-E.

To identify the identities of the cell clusters obtained from the aforementioned clustering, we initially screened for marker genes within each cell cluster. Subsequently, we visualized the expression distribution of these marker genes through heatmaps and UMAP, as illustrated in Fig. S3. By annotating cells based on the marker genes of each cell and the marker genes of each cell cluster, we identified 12 cell types, namely adipocytes, CM, endocardial_cells, endothelial_cells, epicardial_cells, fibroblasts, lymphatics, Macrophages, mast_cells; neuronal_cells; pericytes; and T_cells (Fig. 1A–B). The expression distribution of marker genes for each cell type is shown in Fig. 1C and Fig. S4. Additionally, we displayed the expression patterns of marker genes used to identify cells among the cell subtypes and clusters in Fig. S5, indicating the accurate cell identification outcomes of this study. Different cell types can be clearly distinguished based on classic marker gene expression.

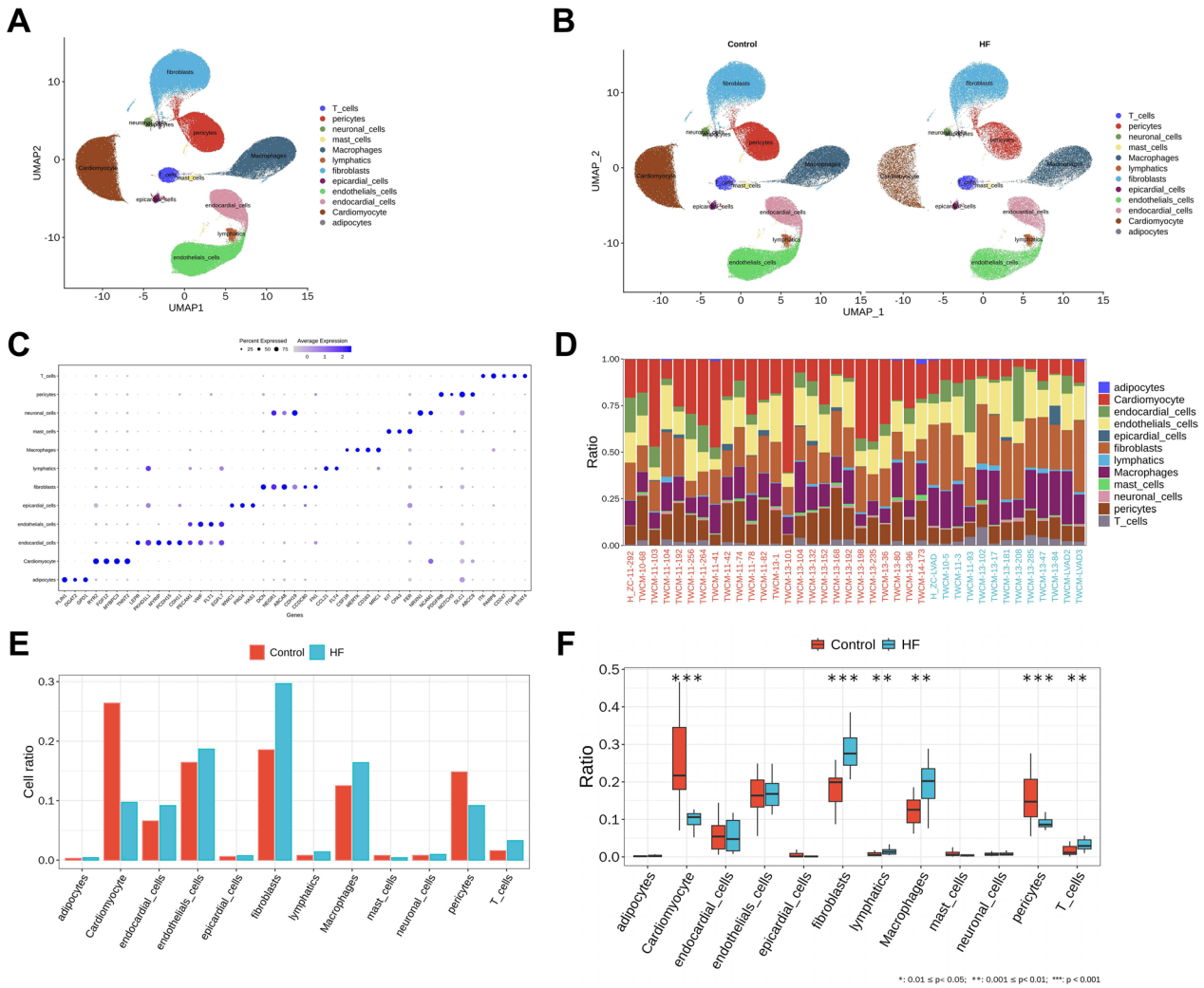

Fig. 1 Cell Type Distribution and Expression Features of scRNA-seq Data. **A** Visualization of cell annotation results grouped based on UMAP clustering, where each color represents a specific cell type; **B** Visualization of cell annotation results based on UMAP clustering, with each color representing a distinct cell type, left panel for the Control group (n = 28), right panel for the HF group (n = 17); **C** Expression patterns of known lineage-specific marker genes across different cell types in Control and HF groups, with darker blue indicating higher average expression levels and larger circles representing more cells expressing the gene; **D** Proportional distribution of cell types in each sample, with each color representing a specific cell type; **E** Bar graph comparison of cell numbers for each cell type, where red represents the Control group (n = 28) and blue represents the HF group (n = 17); **F** Box plot showing changes in cell type proportions, with red indicating the Control group (n = 28) and blue indicating the HF group (n = 17), * denotes statistical significance compared to the Control group, $^{**}p < 0.01$, $^{***}p < 0.001$

Furthermore, we elaborated on the cellular composition distributions within different groups of the 12 cell subtypes (Fig. 1D). Using a Wilcox. For the test, we conducted an analysis to identify changes in cell proportions in the HF group compared to the control group. The analysis revealed a significant decrease in the quantities of CMs and pericytes in the HF group, while the numbers of fibroblasts, lymphocytes, macrophages, and T cells showed a significant increase (Fig. 1E–F), aligning with the alterations in cell composition observed in HF.

The scRNA-seq analysis results above indicate that the HF group and control group can be classified into 30 clusters, successfully identifying 12 cell subtypes. Notably, in the HF group, a significant decrease in the quantities of CMs and pericytes was observed, while fibroblasts, lymphocytes, macrophages, and T cells exhibited a significant increase.

Analysis of key cells and their characteristics influencing the progression of HF

To understand the functional differences behind the quantities and variations of CMs, macrophages, and T cells and to identify the cells that play a crucial role along with their expression characteristics, we analyzed scRNA-seq data of three cell types. We re-clustered these three cell types using UMAP analysis, where CMs were re-clustered into two subtypes, namely CM_1 and CM_2. Compared to the Control group, the number of cells in the CM_1 subtype decreased while it increased in the CM_2 subtype (Fig. 2A, Fig. S6). Macrophages were also re-clustered into two subtypes, Macrophages_1 and Macrophages_2. In comparison to the Control group, the number of cells in the Macrophages_1 subtype increased while it decreased in the Macrophages_2 subtype (Fig. 2B, Fig. S7). The T cells were re-clustered into four cell subtypes: NKT (Natural Killer T cells), $CD8^+$ Effector T cells, T memory cells, and Proliferate NKT cells. The changes in the quantity of each T cell subset were not significant (Fig. 2C, Fig. S8).

To further explore the critical roles of various subtypes of the three cell types in the progression of HF, we investigated the intercellular communication mediated by ligand-receptor interactions. Utilizing the R programming language with the "CellChat" package, we analyzed the communication and interactions between cell phenotypes. The analysis revealed that compared to the Control group, in the HF group, there was a decrease in the total number of pathway interactions between CM_1 cells and an increase in the total number of pathway interactions between Macrophages_1 cells. Additionally, the signaling strength received by CM_2 decreased, while it increased for Macrophages_1 and Macrophages_2, with no significant changes in the communication quantity and strength of other cell types (Fig. 2D–E). These findings further underscore the significance of the interaction between CMs and macrophages in the progression of HF.

In order to screen for cell populations regulated by aging, inflammation, and ferroptosis in HF, this study conducted AUCell analysis based on gene signatures related to aging, inflammation, and ferroptosis. Furthermore, Wilcox. The test was utilized to explore the differences in aging, inflammation, and ferroptosis scores between the disease group and the control group. The analysis results indicate that there are significant differences in the aging-related gene AUCell scores among the subtypes of CM_1, CM_2, Macrophages_1, Macrophages_2, NKT, Proliferate_NKT, and $CD8^+$ Effector T cell in the normal and HF groups (Fig. 2F, Fig. S9–S11). Furthermore, significant intergroup differences were observed in the ferroptosis-related gene AUCell scores among the subtypes of CM_1, CM_2, Macrophages_1, and NKT cells (Fig. 2G, Fig. S12–S14), while only Macrophages_1, NKT, and $CD8^+$ Effector T cell subtypes showed significant differences in the inflammation-related gene AUCell scores between groups (Fig. 2H, Fig. S15–S17). Therefore, it is speculated that the aging and ferroptosis related to CMs may influence the occurrence and development of HF.

The research findings above indicate that CMs are crucial cells mediating intercellular communication in the progression of HF. Moreover, aging and ferroptosis related to CMs may play an essential role in the pathological process of HF.

Further screening key genes related to aging and ferroptosis in CMs

To investigate key genes associated with aging and ferroptosis in CMs, we extracted genes from the scRNA-seq dataset of CM_1 and CM_2 cells and performed differential expression analysis. In CM_1 cells, we identified 616 DEGs, among which 277 genes showed high expression in HF samples, and 339 genes showed low expression (Fig. 3A–B). Likewise, in CM_2 cells, we found 947 DEGs, with 368 genes upregulated in HF samples and 579 genes downregulated (Fig. 3C–D).

The DEGs were subjected to GO functional enrichment analysis and KEGG pathway enrichment analysis. The results revealed that in CM_1 cells, the DEGs were

(See figure on next page.)

Fig. 2 Analysis of Key Cell Expression Characteristics. **A** UMAP clustering results showing the distribution of CM_1 and CM_2 cells, with different colors indicating distinct CM subtypes; **B** UMAP clustering results displaying the distribution of Macrophages_1 and Macrophages_2 cells, with different colors representing different macrophage subtypes; **C** UMAP clustering results illustrating the distribution of various T cell subsets, with different colors denoting different T cell subsets; **D** Total number and interaction strength of cell communications in the Control group (n = 28), where the thickness of lines in the network graph represents the number of pathways and the size of circles in the boxplot indicates the strength of interactions; **E** Total number and interaction strength of cell communications in the HF group (n = 17), with similar visualization as in **D**; **F** Differences in AUC scores for CM subtypes, macrophage subtypes, and T cell subsets between HF group (n = 17) and Control group (n = 28) based on an aging gene set; **G** Differences in AUC scores for CM subtypes, macrophage subtypes, and T cell subsets between HF group (n = 17) and Control group (n = 28) based on a ferroptosis gene set; **H** Differences in AUC scores for CM subtypes, macrophage subtypes, and T cell subsets between HF group (n = 17) and Control group (n = 28) based on an inflammation gene set. * denotes statistical significance compared to the Control group, *$p < 0.05$, **$p < 0.01$, ***$p < 0.001$

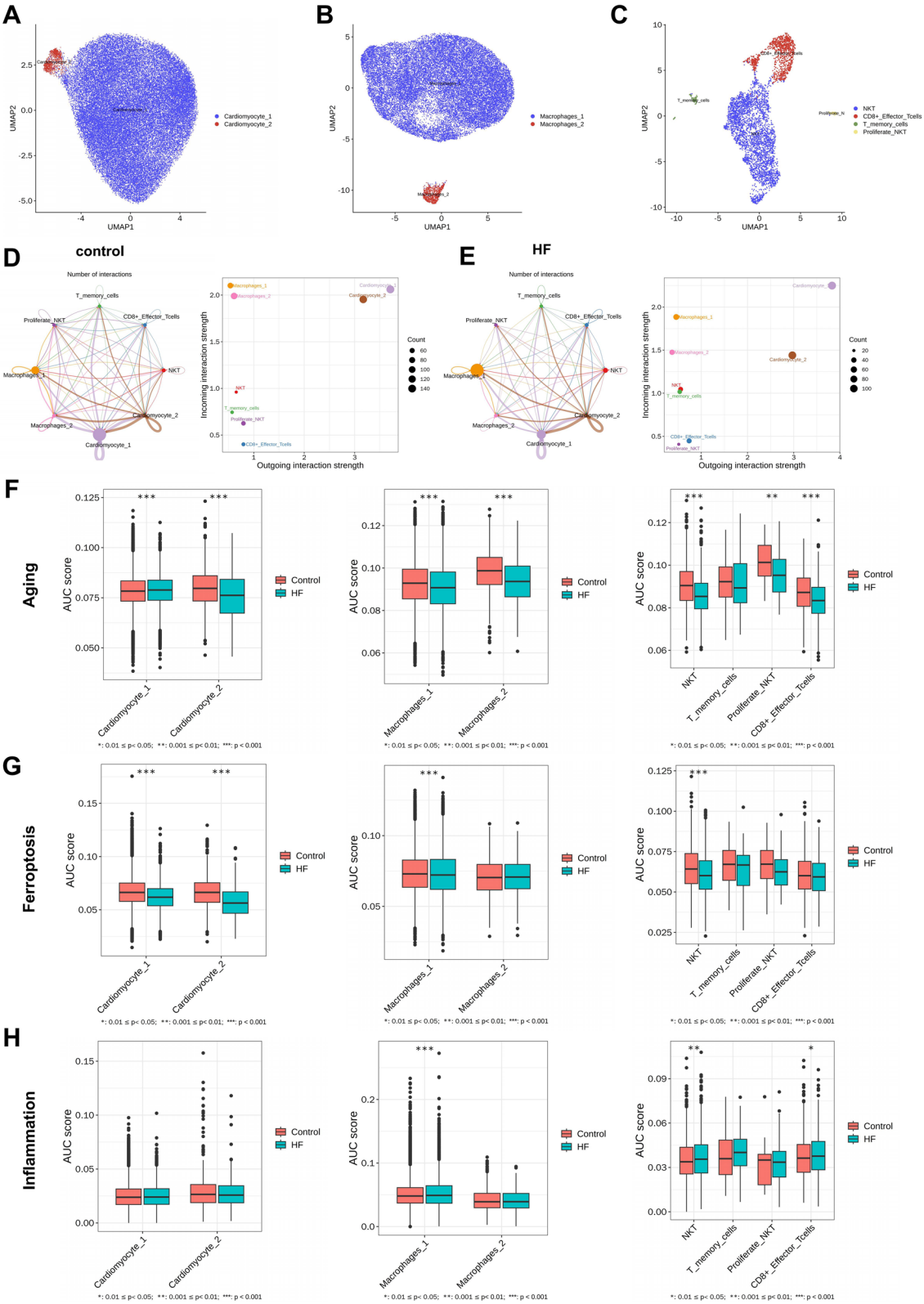

Fig. 2 (See legend on previous page.)

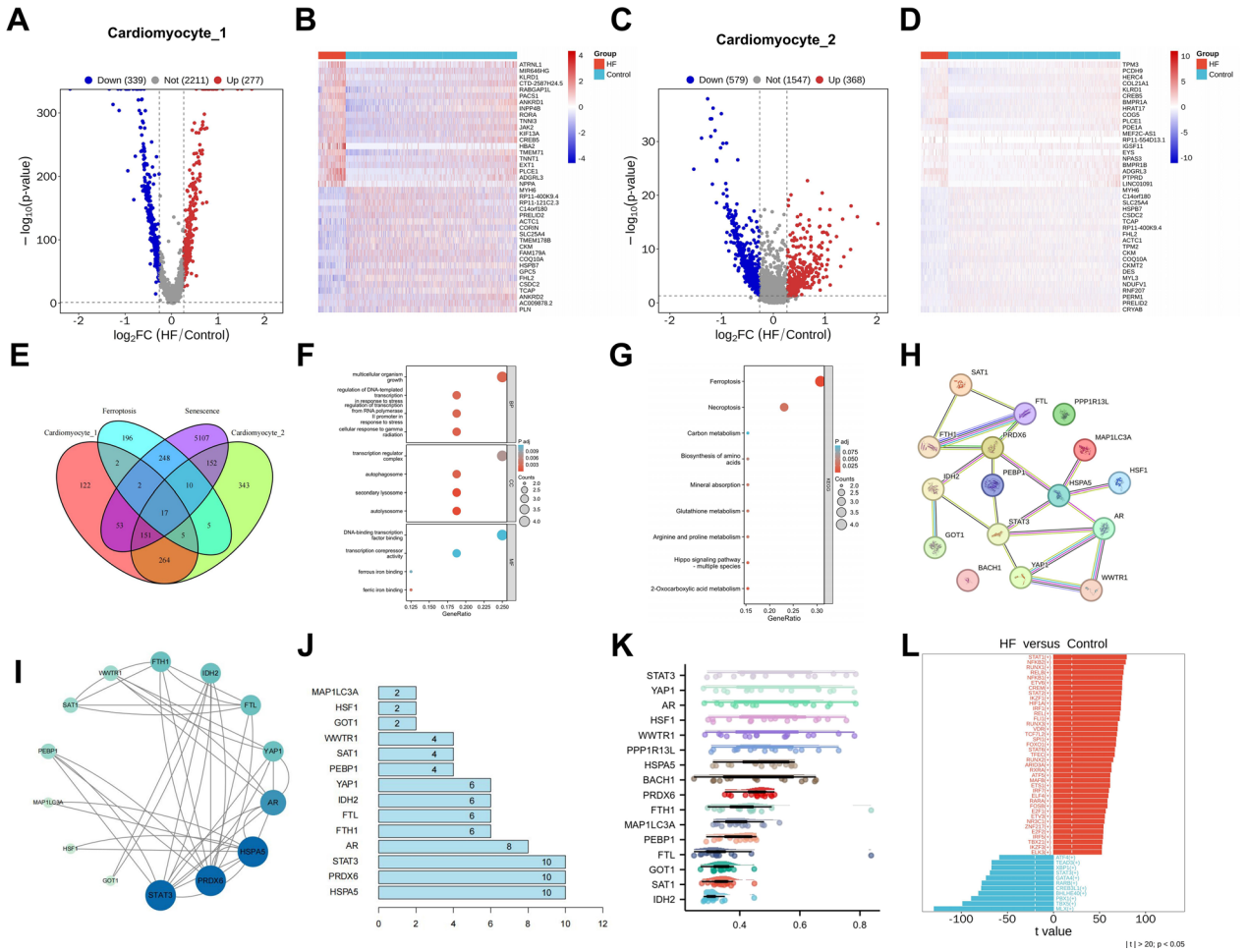

Fig. 3 Identification of Key Genes Associated with Aging and Ferroptosis in CMs. **A** Volcano plot illustrating differential gene expression in CM_1 cells from Control and HF groups, where blue dots to the right of the dotted line represent genes with lower expression in the HF group and red dots to the left indicate genes with higher expression in the HF group; **B** Heatmap showing the expression of the top 20 DEGs in CM_1 cells, with blue indicating downregulation, red indicating upregulation, and darker colors reflecting greater significance of differential expression; **C** Volcano plot displaying differential gene expression in CM_2 cells from Control and HF groups, using a similar color scheme as in (**A**); (**D**) Heatmap presenting the expression of the top 20 DEGs in CM_2 cells, following the color scheme as in (**B**); (**E**) Venn diagram depicting the intersection of DEGs in CM_1 and CM_2 cells, aging-related genes, and ferroptosis-related genes; **F** Bubble plot of GO enrichment analysis for the 17 intersecting genes, with circle color indicating significance of enrichment (from blue to red) and circle size representing the number of enriched genes; **G** Bubble plot of KEGG enrichment analysis for the 17 intersecting genes, using the same visualization as in (F); **H** Protein–protein interaction analysis of the 17 intersecting genes (Combined score = 0.4); **I** PPI network diagram of the 17 intersecting genes, with color gradient from green to blue and circle size indicating the degree value of genes; **J** Statistical analysis of PPI network interaction sites for the 17 intersecting genes, visualized in a graph; **K** Friends analysis of semantic similarity of GO terms among the 17 intersecting genes; **L** Pyscenic analysis of transcription factor regulatory differences in all core cells, highlighting abnormally activated transcription factors in HF samples

associated with BP, including oxidative phosphorylation, aerobic respiration, and cellular respiration (Fig. S18A). In terms of CC, these genes were mainly enriched in the cytoplasm, inner mitochondrial membrane protein complex, and mitochondrial protein-containing complex (Fig. S18B). Regarding MF, the enrichment was primarily observed in oxidoreduction-driven active transmembrane transporter activity, cytoskeletal protein binding, and primary active transmembrane transporter activity (Fig. S18C). Furthermore, the KEGG pathway enrichment analysis indicated that these DEGs were involved in signaling pathways such as Diabetic cardiomyopathy, Oxidative phosphorylation, Thermogenesis, and Prion disease (Fig. S18D).

In CM_2 cells, the DEGs were found to be associated with BP, such as aerobic respiration, cellular respiration, and energy derivation by oxidation of organic compounds (Fig. S19A). The enrichment analysis of CC showed that

these genes were mainly enriched in the cytoplasm, inner mitochondrial membrane protein complex, and intracellular anatomical structure (Fig. S19B). Regarding MF, the enrichment was primarily observed in oxidoreduction-driven active transmembrane transporter activity, cytoskeletal protein binding, and primary active transmembrane transporter activity (Fig. S19C). Additionally, the KEGG pathway enrichment analysis revealed that these DEGs were involved in signaling pathways, including Diabetic cardiomyopathy, Cardiac muscle contraction, Oxidative phosphorylation, and Thermogenesis (Fig. S19D).

The intersection of DEGs in CM_1 and CM_2 cells related to aging and ferroptosis resulted in 17 common genes, namely: BACH1, AR, WWTR1, YAP1, FTL, MAP1LC3A, PEBP1, FTH1, LINC00472, HSPA5, PPP1R13L, GOT1, STAT3, PRDX6, HSF1, SAT1, and IDH2 (Fig. 3E). These 17 intersecting genes exhibited consistent expression trends in both CM_1 and CM_2 cells (Table S1-S2). Subsequently, these 17 intersecting genes were subjected to GO functional enrichment analysis and KEGG pathway enrichment analysis. The analysis revealed that these 17 intersecting genes were associated with BP, such as multicellular organism growth, regulation of DNA-templated transcription in response to stress, and regulation of transcription from RNA polymerase II promoter in response to stress. In terms of CC, these genes were primarily enriched in the transcription regulator complex, autophagosome, and secondary lysosome. Regarding MF, the enrichment was predominantly observed in DNA-binding transcription factor binding, transcription corepressor activity, and ferrous iron binding (Fig. 3F). Furthermore, the KEGG pathway enrichment analysis of these intersecting genes showed their involvement in signaling pathways, including Ferroptosis, Necroptosis, Carbon metabolism, and Biosynthesis of amino acids (Fig. 3G).

Using STRING for protein–protein interaction analysis of the 17 intersecting genes (Fig. 3H), we obtained the PPI network and interaction rankings of these genes, providing detailed information in Fig. 3I–J. STAT3, PRDX6, and HSPA5 genes were identified as having pivotal roles in this protein interaction network. Additionally, we utilized the GOSemSim package to calculate the semantic similarity of GO terms among the 17 intersecting genes. This analysis assessed the functional closeness of these genes by evaluating the shared GO terms they possessed. By comparing the functional similarity among genes, we can identify genes that are significantly associated or functionally aberrant. The analysis revealed that the STAT3 gene exhibited the highest functional similarity (Fig. 3K), suggesting its potential central role in the corresponding BP. Furthermore, we analyzed the differential regulation of all core cell transcription factors, and by grouping, we further selected transcription factors that were abnormally activated in HF samples. The analysis showed significant inhibition of the activation of the STAT3 factor in HF samples (Fig. 3L).

These research findings indicate that the expression regulation of the STAT3 gene in CMs of HF samples may play a crucial role in the occurrence and development of HF, with STAT3 potentially being significantly associated with the aging and ferroptosis of CMs.

Activation of STAT3 inhibits CMs ferroptosis and promotes functional repair

To further investigate the impact of the STAT3 gene on the biological functions of CMs and cell ferroptosis, we designed three shRNA sequences targeting STAT3. We constructed STAT3 silenced and overexpressed CMs through lentiviral transfection of these sequences individually (Fig. 4A). Transfection efficiency was validated using RT-qPCR and Western blot, and the sequence sh-STAT3-3, showing the most optimal transfection efficiency, was selected for subsequent experiments (Fig. S20).

Next, we conducted experiments to assess the changes in the biological functions of CM cells in different intervention groups. Results from CCK8 and EDU assays revealed that compared to the sh-NC group, the sh-STAT3 group exhibited significantly reduced cell viability and proliferation capabilities. In contrast, when compared to the oe-NC group, the oe-STAT3 group demonstrated significantly enhanced cell viability and proliferation abilities (Fig. 4B–D). Apoptosis levels were assessed by flow cytometry, showing that silencing STAT3 induced increased apoptosis in CMs cells, while overexpressing SIRT1 inhibited CMs cell apoptosis (Fig. 4E). The results from Transwell and wound healing assays indicated that, compared to the sh-NC group, the migration ability of CMs cells in the sh-STAT3 group was significantly weakened, while in comparison to the oe-NC group, the migration capability of CMs cells in the oe-STAT3 group was notably increased (Fig. 4F–G). These experimental findings suggest that silencing STAT3 in CM cell lines inhibits cell proliferation and migration while promoting CM cell apoptosis. On the other hand, overexpressing STAT3 enhances cell proliferation and migration while suppressing cell apoptosis.

Initially, we investigated the regulatory role of STAT3 in iron balance by analyzing the expression of iron metabolism-related genes using the FerroOrange probe. As shown in (Fig. 5A–B), within 24 h of knocking down STAT3, an increase in intracellular Fe^{2+} content was observed, while overexpressing STAT3 led to a significant reduction in intracellular Fe^{2+} levels.

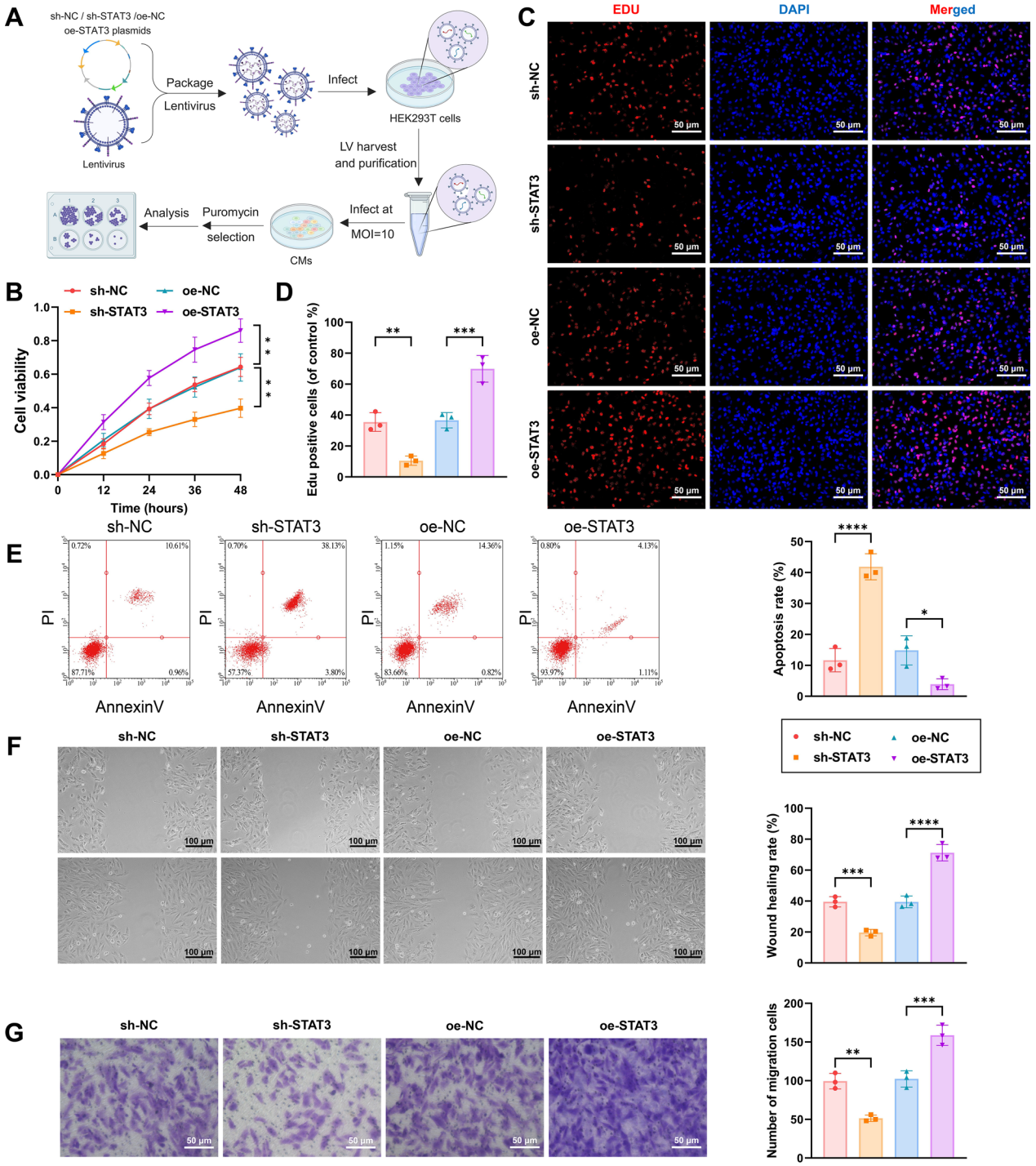

Fig. 4 Impact of STAT3 Gene on the Biological Functions of CMs. **A** Schematic diagram of experimental procedure involving lentivirus transfection for silencing or overexpression of STAT3; **B** Viability changes of CMs in different intervention groups at 12, 24, 36, and 48 h detected by CCK-8 assay; **C** Assessment of proliferative capacity of CMs in different intervention groups using EDU experiment, with EDU-positive cells shown in red indicating cells in the proliferative phase, and blue representing DAPI-stained cell nuclei (scale bar = 50 μm); **D** Statistical analysis of EDU staining results; **E** Assessment of apoptosis in CMs in different intervention groups using Annexin V/PI double staining flow cytometry, with the bar graph showing the percentage of cells in Q2 and Q3 quadrants indicating apoptotic cells; **F** Evaluation of migration of CMs in different intervention groups using wound healing assay (scale bar = 100 μm); **G** Evaluation of migration capacity of CMs in different intervention groups using Transwell assay (scale bar = 50 μm). Quantitative data in the figures are presented as Mean ± SD. Each cell experiment was repeated 3 times. * denotes comparison between two groups, $^{**}p < 0.01$, $^{***}p < 0.001$, $^{****}p < 0.0001$

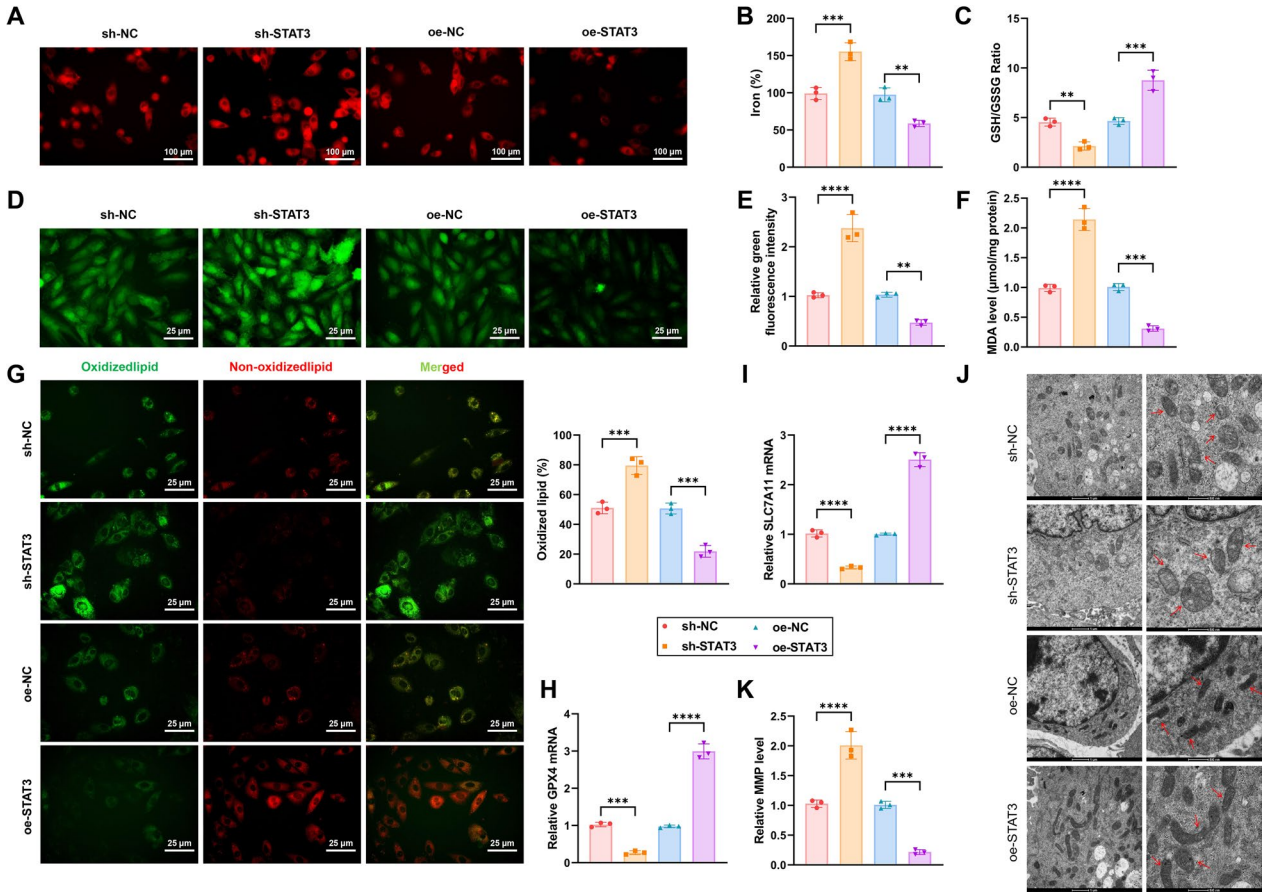

Fig. 5 Influence of STAT3 on CMs Cell Ferroptosis. **A** Representative fluorescence images of CMs transfected with different lentiviruses for intracellular iron levels identified using FerroOrange (Scale bar = 100 μm); **B** Statistical analysis of iron content in CMs from different intervention groups using assay kits; **C** GSH/GSSG ratio in CMs from different intervention groups; **D**–**E** Visualization of ROS production in CMs using DCFH-DA under confocal laser scanning microscopy and statistical analysis using flow cytometry (Scale bar = 25 μm); **F** Measurement of MDA content in different intervention groups; **G** Representative confocal images of CMs stained with C11-BODIPY 581/591. Red indicates unoxidized lipids, while green represents oxidized lipids (Scale bar = 25 μm); **H**–**I** Transcription levels of ferroptosis-related genes SLC7A11 and GPX4 detected by RT-qPCR; **J** Observation of mitochondrial morphology in cells using TEM, with red arrows pointing to mitochondrial structures (scale bar = 1 μm); **K** Detection of mitochondrial membrane potential (MMP: mitochondrial membrane potential) in cells from different intervention groups using JC-1 assay. Quantitative data in the figures are presented as Mean ± SD. Each cell experiment was repeated 3 times. * denotes comparison between two groups, $^{**}p < 0.01$, $^{***}p < 0.001$, $^{****}p < 0.0001$

To further validate the impact of STAT3 on redox balance, we compared oxidative stress indicators and peroxidation products. In the sh-STAT3 group, a significant decrease in the GSH/GSSG ratio was observed, while in the oe-STAT3 group, the GSH/GSSG ratio significantly increased, indicating a mitigation of oxidative stress levels (Fig. 5C). Confocal laser scanning microscopy examination and flow cytometry fluorescence quantification results both demonstrated that CM cells treated with STAT3 knockdown exhibited an increase in ROS production, whereas cells overexpressing STAT3 showed a significant reduction in ROS generation (Fig. 5D–E).

The results indicated that, compared to the sh-NC group, the sh-STAT3 group exhibited a significant increase in MDA levels, while the oe-STAT3 group showed a marked decrease in MDA levels when compared to the oe-NC group (Fig. 5F). Evaluation of lipid peroxidation levels using C11-BODIPY581/591 also revealed a significant upregulation after STAT3 knockdown and downregulation after STAT3 overexpression (Fig. 5G). Compared to the sh-NC group, the sh-STAT3 group showed a significant decrease in mRNA transcription levels of GPX4 and SLC7A11, while the oe-STAT3 group exhibited a significant increase in mRNA transcription levels of GPX4 and SLC7A11 when compared to the oe-NC group (Fig. 5H–I).

Ferroptosis is accompanied by characteristic mitochondrial morphological changes [34, 35]. As depicted

in Fig. 5J, the sh-STAT3 group of CMs displayed mitochondrial shrinkage, reduced cristae, and increased membrane density, while the oe-STAT3 group of CMs exhibited mitochondrial damage repair. Assessment of mitochondrial membrane potential using JC-1 revealed that knocking down STAT3 significantly increased mitochondrial membrane potential hyperpolarization in CMs, whereas overexpressing STAT3 markedly decreased mitochondrial membrane potential hyperpolarization in CMs (Fig. 5K), suggesting that STAT3 may influence ferroptosis in CMs by impacting mitochondrial function. In conclusion, these results confirm the involvement of STAT3 in regulating and inhibiting ferroptosis in CMs.

Overall, the study results indicate that STAT3 is involved in regulating and inhibiting ferroptosis in CMs, thus promoting the growth, proliferation, and migration of CMs while inhibiting cell apoptosis.

Successful preparation of PN@Col

We synthesized a novel antioxidant PN by combining EGCG with glycine (Gly) and loaded the STAT3 agonist Colivelin into this nanoparticle, named PN@Col [36, 37] (Fig. 6A). Subsequently, we employed TEM to observe the shape and structure of the nanoparticles. As depicted in Fig. 6B, the prepared nanoparticles are likely to be spherical in three-dimensional space, with PN@Col particles relatively larger than PN particles. Further confirmation from SEM images revealed that the prepared nanoparticles are spherical and that lipid particles increased in size after Colivelin loading (Fig. 6C). Particle size analysis provided additional verification, as the nanosizer detected that the average diameter of PN was 112.62 ± 8.67 nm, with a Zeta potential of -31.28 mV, whereas the average diameter of PN@Col was 226.71 ± 16.92 nm, with a Zeta potential of -18.66 mV. Compared to PN, PN@Col exhibited a slightly higher Zeta potential and a slight increase in diameter (Fig. 6D–E), indicating that PN@Col exhibits good integrity. Subsequently, we used high-performance liquid chromatography (HPLC) to confirm the successful drug loading by measuring the drug loading capacity and encapsulation efficiency. The results indicated that PN@Col successfully loaded Colivelin, with a Colivelin content of 12.6 ± 1.5% (n = 6) and an encapsulation efficiency of 69.7 ± 13.2%. We then evaluated its in vitro release profile in PBS (pH 7.4) containing 0.1% Tween 80. The results showed that 11–12% and 76–83% of the loaded Colivelin were released after 3 h and 24 h, respectively, with no further release observed in the subsequent 48 h (Fig. 6F).

We evaluated the viability of cells treated with different nanoparticles using fluorescence microscopy. The results demonstrated a significant increase in the survival rate of CM cells in the PN@Col treatment group compared to the PN treatment group (Fig. 6G). Furthermore, we assessed the radical scavenging ability and antioxidant activity of PN@Col by measuring DPPH and ABTS free radicals. The results indicated that both PN and PN@Col exhibited strong radical scavenging abilities (Fig. 6H). Using Trolox as the reference antioxidant for the ABTS assay to quantify the antioxidant capacity and express it as equivalent antioxidant capacity, the calculations revealed that both PN and PN@Col possessed robust antioxidant capabilities (Fig. 6I). Importantly, the loading of Colivelin did not affect the radical scavenging and antioxidant abilities of PNs.

These findings collectively demonstrate the successful development of a polyphenol nanoparticle loaded with a STAT3 agonist (PN@Col).

PN@Col inhibits CMs ferroptosis and promotes functional recovery

To investigate the impact of PN@Col on the biological functions of CMs, we induced ferroptosis in CMs by treating them with Erastin, followed by treatment with nanoparticles and assessment of their biological functions. Initially, Western blot analysis revealed that compared to the control group, the expression of p-STAT3 protein in CM cells was significantly downregulated in the Erastin-treated group. However, following treatment with Colivelin and PN@Col, there was an upregulation of p-STAT3 protein expression in the cells, with PN@Col demonstrating a stronger upregulation capacity (Fig. 7A). Results from CCK-8 and EDU staining assays indicated that compared to the control group, the viability and proliferative capacity of CM cells in the Erastin-treated group significantly decreased. However, following treatment with Colivelin and PN@Col, there was a partial recovery in both cell viability and proliferative capacity, with the PN@Col treatment group showing the most pronounced recovery effects (Fig. 7B–C). The study findings from cell scratch and Transwell assays demonstrate that Erastin suppresses the migration ability of CMs. Furthermore, compared to the control group treated with unloaded drug nanoparticles (PNs), the addition of Colivelin and PN@Col shows a partial restoration of cell migration capability. Particularly, the cell migration ability is significantly enhanced in the PN@Col treatment group (Fig. 7D–E).

Subsequently, we assessed the apoptosis of CM cells treated with different reagents using flow cytometry. The results revealed that Erastin could induce apoptosis in CM cells. However, treatment with Colivelin and PN@Col inhibited apoptosis in the cells, with PN@Col demonstrating a significantly stronger capacity to suppress apoptosis compared to Colivelin (Fig. 7F).

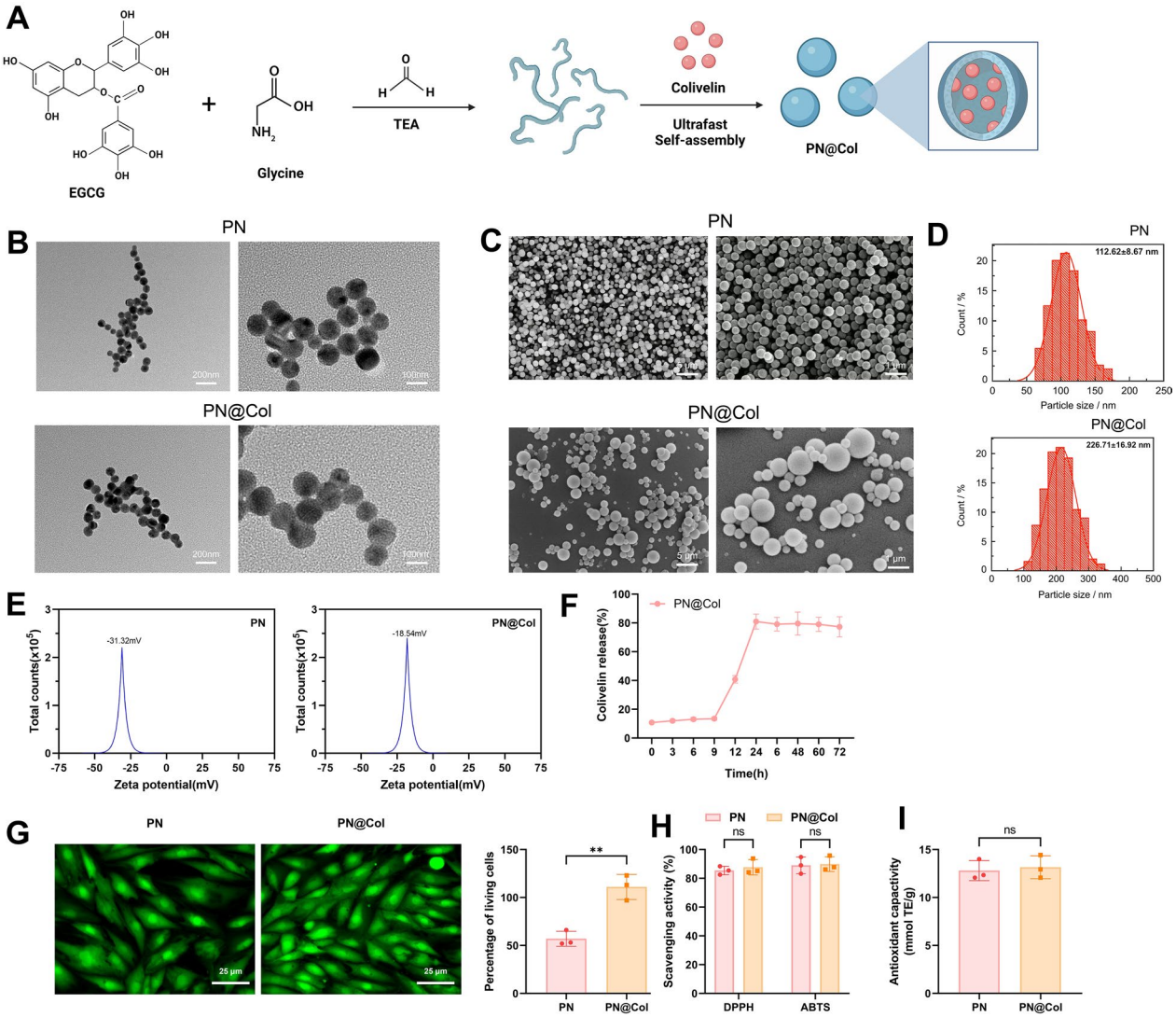

Fig. 6 Synthesis and Characterization of Novel Antioxidant PNs. **A** Schematic diagram of the synthesis steps of PN@Col nanoparticles; **B** Morphological features of PN (top) and PN@Col (bottom) observed using TEM (scale bar: 100 nm/200 nm); **C** Morphology of PN (top) and PN@Col (bottom) observed using SEM (scale bar: 5 μm/1 μm); **D** Particle size distribution of PN (left) and PN@Col (right) analyzed by nanoparticle tracking; **E** Zeta potential analysis of PN (left) and PN@Col (right) by nanoparticle tracking; **F** In vitro release of Colivelin from PN@Col nanoparticles. No significant differences were observed between samples at each time point. Data are presented as the mean with a standard deviation from three independent samples prepared under the same conditions; **G** Fluorescence microscopy images of CMs cells cultured with PN (left) and PN@Col (right) for 24 h, with green fluorescence staining indicating viable cells (scale bar = 25 μm); (H) DPPH and ABTS radical scavenging activities of PN and PN@Col; **I** Antioxidant capacity assessment of PN and PN@Col. Quantitative data in the figures are presented as Mean ± SD. Each experiment was repeated 3 times. "ns" indicates no statistically significant difference between the two groups

Further detection of ferroptosis-specific indicators revealed significant differences: compared to the control group, the model and PNs groups exhibited elevated levels of intracellular Fe^{2+}, ROS, lipid peroxidation, and MDA in CMs, along with a significant decrease in GSH/GSSG ratio. In contrast, the colivelin and PN@Col groups showed significant reductions in intracellular Fe^{2+}, ROS, MDA levels, and lipid peroxidation compared to the model group. Additionally, the GSH/GSSG ratio was significantly increased in these groups. Furthermore, the PN@Col group demonstrated a significantly greater ability to restore ferroptosis-specific indicators compared to the colivelin group (Fig. 7G-K).

To further validate our findings, we examined the expression of GPX4 and SLC7A11 mRNA. The RT-qPCR results revealed that compared to the control group, the model and PNs groups exhibited a significant decrease in mRNA expression levels of GPX4 and SLC7A11. In

contrast, the colivelin and PN@Col groups showed a notable restoration in the expression levels of GPX4 and SLC7A11 compared to the model and PNs groups. Importantly, PN@Col demonstrated a significantly greater ability to restore their expression compared to colivelin (Fig. 7L-M).

Additionally, as illustrated in Fig. 7N, compared to the control group, the model and PNs groups displayed mitochondrial shrinkage, reduced cristae, and increased membrane density. Conversely, the colivelin and PN@Col groups exhibited mitochondrial repair, increased cristae, and reduced membrane density relative to the model group. Importantly, PN@Col showed a significantly stronger capacity to repair mitochondrial damage compared to colivelin. The results of the JC-1 assay assessing mitochondrial membrane potential changes revealed that the mitochondrial membrane potential hyperpolarization in CMs was notably elevated in the model group compared to the control group. In contrast, both the colivelin and PN@Col groups showed a significant reduction in mitochondrial membrane potential hyperpolarization compared to the model and PNs groups, with PN@Col demonstrating a significantly superior ability to restore the mitochondrial membrane potential compared to colivelin (Fig. 7O).

These research findings indicate that PN@Col antioxidant PNs can inhibit ferroptosis in CMs, regulate biological functions, promote functional recovery, and suppress cell apoptosis.

PN@Col significantly improves cardiac function in age-related HF mice

To investigate the impact of PN@Col on cardiac function in age-related HF mice further, we validated the HF elderly mouse model constructed through transverse aortic constriction surgery and treated them through tail vein injection of nanoparticles. After 28 days of treatment, the mice in each group underwent an assessment of cardiac functional parameters.

The results of the ultrasound diagnostic equipment revealed that compared to the sham group, mice in the model and PNs groups exhibited significantly increased IVSD, LVEDD, and LVESD, as well as decreased LVPW'T, LVEF, and LVFS. In comparison to the model and PNs groups, mice in the colivelin and PN@Col groups displayed significant reductions in IVSD, LVEDD, and LVESD, while LVPWD, LVEF, and LVFS showed significant increases. Additionally, the therapeutic effect of PN@Col was significantly more pronounced than that of Colivelin (Fig. 8A–B; Fig. S21A–F).

Hemodynamic assessment results demonstrated that compared to the sham group, mice in the model group exhibited a significant increase in LVEDP and a significant decrease in LVSP, maximal rate of pressure rise in the left ventricle (+dP/dt), and maximal rate of pressure decrease in the left ventricle (-dP/dt). In comparison to the model and PNs groups, mice in the colivelin and PN@Col groups showed a significant reduction in LVEDP, while LVSP, maximal rate of pressure rise, and maximal rate of pressure decrease in the left ventricle significantly increased (Fig. S21G–J). The examination of ventricular mass index revealed that relative to the sham group, mice in the model group had significantly increased left and right ventricular mass indices (LVMI and RVMI). In contrast, compared to the model and PNs groups, mice in the colivelin and PN@Col groups displayed a significant decrease in LVMI and RVMI, with PN@Col demonstrating a significantly greater capacity to restore cardiac function in mice than Colivelin (Fig. S21K–L).

Following the euthanasia of mice, the hearts were harvested and subjected to H&E staining. Results revealed that compared to the sham group, the hearts of mice in the model and PNs groups exhibited significant hypertrophy with a noticeable increase in cross-sectional area.

(See figure on next page.)

Fig. 7 Impact of PN@Col on the Biological Functions of CMs. **A** Expression changes of p-STAT3 protein in CMs cells from different treatment groups detected by Western blot; **B** Viability changes of CMs in different treatment groups at 12, 24, 36, and 48 h assessed by CCK-8 assay; **C** Evaluation of proliferative capacity of CMs in different treatment groups using EDU experiment, with red fluorescence indicating EDU-positive cells in the proliferative phase and blue fluorescence representing DAPI-stained cell nuclei (scale bar = 50 μm); **D** Assessment of cell migration in different intervention groups of CMs using wound healing assay (scale bar = 100 μm); **E** Evaluation of migration capacity of CMs in different treatment groups using Transwell assay (scale bar = 50 μm); **F** Detection of apoptosis in CMs from different treatment groups using Annexin V/PI double staining flow cytometry, with bar graph representing the percentage of cells in Q2 and Q3 quadrants indicating apoptotic cells; **G** Representative fluorescence images of intracellular iron levels in CMs from different treatment groups identified using FerroOrange (Scale bar = 25 μm); **H** Visualization of ROS production in CMs using DCFH-DA under confocal laser scanning microscopy and statistical analysis using flow cytometry (Scale bar = 25 μm); **I** Representative confocal images of CMs stained with C11-BODIPY 581/591. Red indicates unoxidized lipids, while green represents oxidized lipids (Scale bar = 25 μm); **J** GSH/GSSG ratio in CMs from different treatment groups; **K** Measurement of MDA content in CMs from different treatment groups; **L**–**M** Transcription levels of ferroptosis-related genes SLC7A11 and GPX4 detected by RT-qPCR; **N** Observation of mitochondrial morphology in cells using TEM, with red arrows indicating mitochondrial structures (scale bar = 1 μm); **O** Detection of mitochondrial membrane potential (MMP) in cells from different treatment groups using JC-1 assay. Quantitative data in the figures are presented as Mean ± SD. Each cell experiment was repeated 3 times. * denotes comparison between two groups, *$p < 0.05$, **$p < 0.01$, ***$p < 0.001$, ****$p < 0.0001$

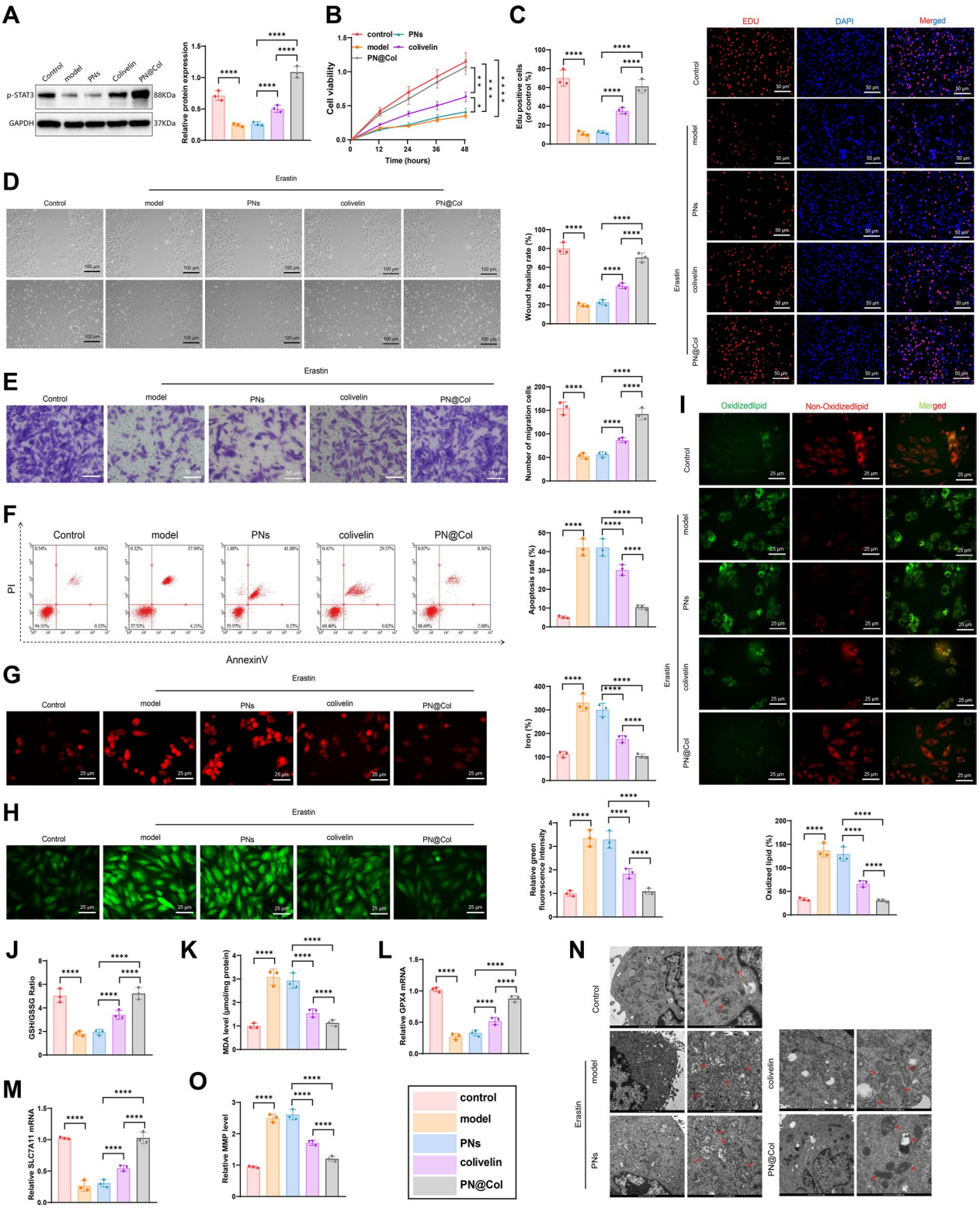

Fig. 7 (See legend on previous page.)

Treatment with Colivelin and PN@Col alleviated cardiac hypertrophy in mice post-treatment, with PN@Col demonstrating superior ability in restoring heart size compared to Colivelin (Fig. 8C–D). Utilizing WGA staining, we measured the cross-sectional area of CMs. Our study findings indicated a significant increase in CM cross-sectional area in the model and PNs groups mice, which was mitigated by treatment with Colivelin and PN@Col, with PN@Col showing a more favorable therapeutic effect (Fig. 8E).

Additionally, we conducted a comprehensive in vivo toxicity assessment. HE staining analysis of the kidney and liver revealed no significant damage after PN@Col injection (Fig. S22A). Cytokine levels measured by ELISA indicated that PN@Col injection did not trigger harmful inflammatory responses (Fig. S22B).

Results from Sirius Red staining and Masson's trichrome staining demonstrated a significant increase in interstitial fibrosis deposition area in the myocardium of mice in the model and PNs groups compared to the sham group. However, following treatment with Colivelin and PN@Col, the degree of fibrosis notably decreased, with PN@Col exhibiting stronger inhibitory capacity against myocardial fibrosis (Fig. 8F). The process of myocardial hypertrophy is accompanied by complex changes in gene expression levels, which are causally linked to the occurrence and progression of the hypertrophic phenotype. BNP, β-MHC, and collagen I gene re-expression during myocardial hypertrophy is well recognized [38, 39]. Therefore, simultaneous detection of BNP, β-MHC, and collagen I gene expression will be of great significance for determining myocardial hypertrophy and its prognosis. Western blotting showed that, compared to the sham group, BNP, β-MHC, and collagen I protein levels were significantly increased in the hearts of the model and PNs groups. After treatment with Colivelin and PN@Col, these protein levels were alleviated, with the reduction in BNP, β-MHC, and collagen I protein levels in the PN@Col group being significantly stronger than that in the Colivelin group (Fig. 8G). TUNEL staining confirmed that both Colivelin and PN@Col could suppress apoptosis of CMs in HF mice, with PN@Col showing a more pronounced inhibitory effect (Fig. 8H).

Furthermore, we evaluated the expression of p-STAT3 protein in the cardiac tissues of mice from different treatment groups. Analysis revealed a decrease in p-STAT3 protein expression in the myocardial tissues of mice in the model and PNs groups compared to the sham group. In contrast, treatment with Colivelin and PN@Col led to a significant upregulation of p-STAT3 protein expression compared to the model group, confirming the ability of PN@Col to activate STAT3 (Fig. 8I).

In addition, we assessed specific markers of ferroptosis, revealing that compared to the sham group, mice in the model group exhibited a significant increase in Fe^{2+}, ROS, and MDA levels in cardiac tissues, accompanied by a notable decrease in the GSH/GSSG ratio. Conversely, compared to the model and PNs groups, the cellular levels of Fe^{2+}, ROS, and MDA in the Colivelin and PN@Col groups markedly decreased, while the GSH/GSSG ratio significantly increased. Furthermore, the PN@Col group demonstrated a significantly stronger ability to restore specific markers of ferroptosis compared to the Colivelin group (Fig. 8J–M).

To further validate our findings, we examined the expression of Gpx4 and Slc7a11 mRNA. Results from RT-qPCR demonstrated that compared to the sham group, the mRNA levels of Gpx4 and Slc7a11 in the model and PNs groups showed a significant decrease. In contrast, the expression levels of Gpx4 and Slc7a11 in the Colivelin and PN@Col groups exhibited a noticeable restoration compared to the model group,

(See figure on next page.)

Fig. 8 Impact of PN@Col on Age-related HF Mouse Cardiac Function. **A** Representative cardiac ultrasound images of mice in different treatment groups; **B** Representative left ventricular pressure waveforms, with a scale of 40 mmHg vertically and 100 ms horizontally; **C** Anatomical diagrams of mouse hearts from different treatment groups; **D** H&E stained images of mouse heart tissues from different treatment groups, with quantification of cross-sectional area of the heart tissues(scale bar: 500 μm/50 μm); **E** Assessment of CM size with WGA staining results (scale bar: 50 μm); **F** Evaluation of myocardial interstitial fibrosis deposition in mouse ventricles with Sirius Red staining (left) and Masson staining (right), where CVF (Collage Volume Fraction) quantifies the ratio of Masson-stained blue area to total heart chamber area (scale bar: 500 μm/50 μm), fibrotic area in mice indicated by picro sirius red-positive area (scale bar: 50 μm); **G** Western blot analysis of BNP, β-MHC, and collagen I protein expression changes in heart tissues from different treatment groups; (H) TUNEL staining detecting apoptosis in mouse myocardial tissue, with red fluorescence representing apoptotic cells and blue fluorescence from DAPI nuclear staining (scale bar: 50 μm); **I** Immunohistochemical staining to assess the expression of p-STAT3 protein in mouse heart tissues (scale bar: 50 μm); **J** Prussian blue staining for detecting iron ion content in mouse heart tissue (scale bar: 50 μm); **K** Detection of ROS levels in mouse heart tissues from different treatment groups; **L** Assessment of GSH/GSSG ratio in mouse heart tissues from different treatment groups; **M** Measurement of MDA content in mouse heart tissues from different treatment groups; **N** RT-qPCR analysis of transcription levels of ferroptosis-related genes Slc7a11 and Gpx4 in mouse heart tissues from different treatment groups; **O** Representative TEM images of mouse heart tissues from different treatment groups(scale bar: 2 μm). Quantitative data in the figures are presented as Mean ± SD, with 6 mice per group in each experiment, where * represents a comparison between two groups, ** indicates $p < 0.01$, *** indicates $p < 0.001$, and **** indicates $p < 0.0001$

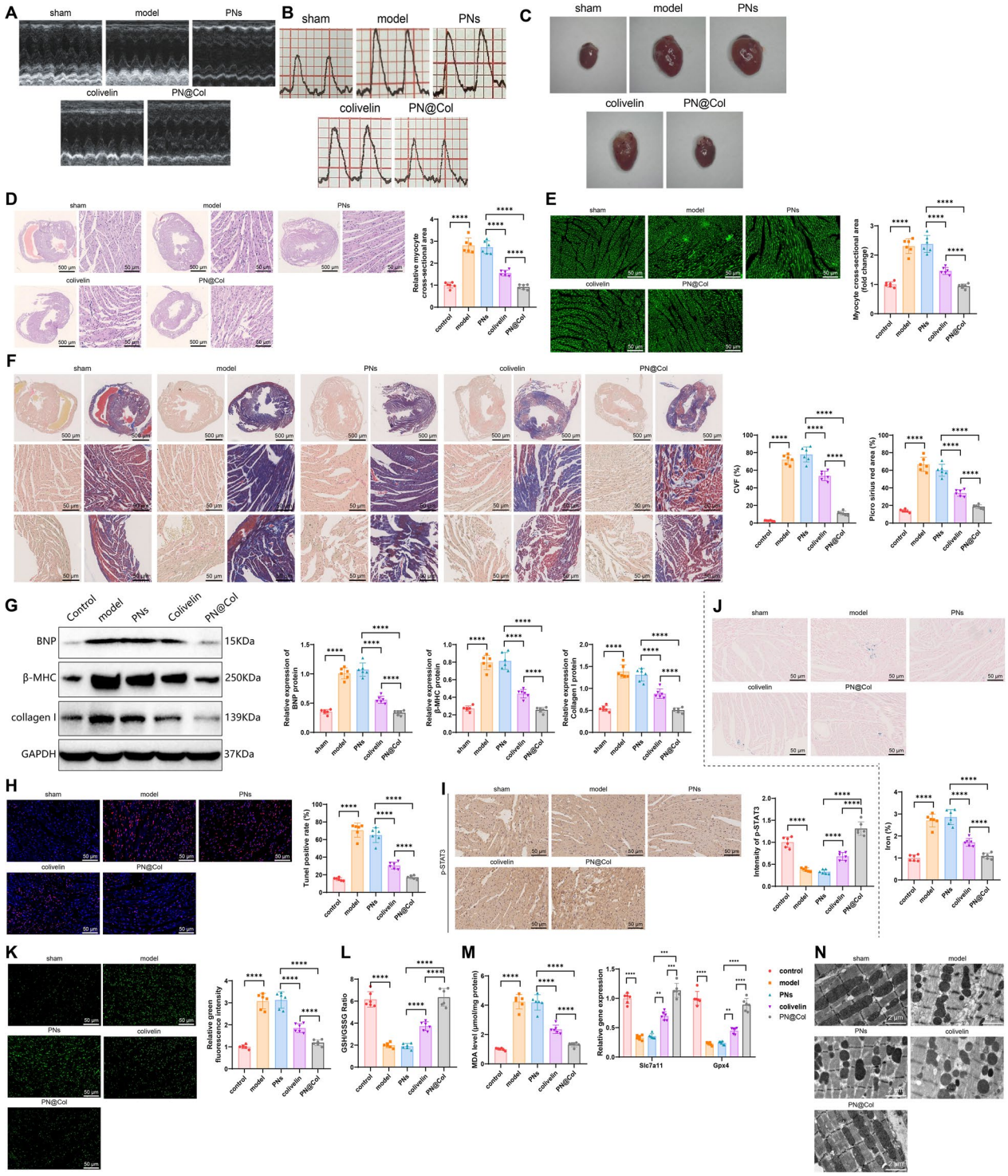

Fig. 8 (See legend on previous page.)

with PN@Col showing a significantly stronger ability to restore their expression levels than Colivelin (Fig. 8N). TEM revealed typical mitochondrial abnormalities associated with ferroptosis in the model group, including mitochondrial ridge destruction and membrane integrity impairment. Following treatment with Colivelin and PN@Col, the aforementioned ultrastructural damages were alleviated, with PN@

Col demonstrating a superior therapeutic effect over Colivelin (Fig. 8O).

The results of the study indicate that PN@Col treatment can significantly improve cardiac function in HF mice by inhibiting CM ferroptosis.

HF is a fatal cardiac disease that poses a significant threat to global health due to its high incidence and mortality rates [40, 41]. Oxidative stress and ferroptosis have been widely recognized as important pathological mechanisms in the progression of HF [42, 43]. Against this background, this study aims to explore a novel therapeutic strategy utilizing PN@Col to improve age-related HF. The findings indicate that PN@Col not only effectively suppresses oxidative stress and ferroptosis but also significantly enhances cardiac function in mice with HF. The comprehensive application of scRNA-seq analysis, in vitro cell experiments, and in vivo mouse models validates the potential of PN@Col in the treatment of HF.

Previous studies have indicated that oxidative stress plays a critical role in the occurrence and development of HF, and conventional antioxidants and iron chelators can, to some extent, slow the progression of the condition [44, 45]. However, these treatment methods often have issues such as low bioavailability and poor targeting. In contrast, the PN@Col used in this study offers higher stability and specificity. Unlike traditional antioxidants, PN@Col can stably exist within cells and effectively deliver a STAT3 agonist to CMs, significantly enhancing the therapeutic effects. Furthermore, PN@Col demonstrates multiple synergistic actions by not only directly scavenging free radicals but also regulating the ferroptosis pathway, further protecting CMs.

STAT3 is a crucial transcription factor extensively involved in processes such as cell proliferation, differentiation, apoptosis, and immune response [46, 47]. Previous studies have confirmed the essential role of STAT3 in the pathological progression of HF, with its activation significantly reducing ferroptosis and inflammation in CMs [46, 48]. Through scRNA-seq analysis, this study further validates the key role of STAT3 in HF. In vitro experimental results demonstrate that the STAT3 agonist markedly enhances CM viability, suppresses ferroptosis, and improves cellular biological functions. In comparison to other studies, the utilization of a nanoparticle delivery system in this study enhances the bioavailability and therapeutic effects of the STAT3 agonist [49–51].

PN@Col significantly improves the condition of HF by inhibiting ROS generation and regulating ferroptosis. In vitro experiments demonstrate that PN@Col effectively reduces ROS levels in CMs, decreasing the damage caused by oxidative stress. Additionally, PN@Col significantly reduces the rate of ferroptosis in CMs by modulating the relevant signaling pathways. In vivo, experiments further validate the therapeutic effects of PN@Col, as mice models receiving PN@Col injections show a substantial improvement in cardiac function, as well as a noticeable reduction in the hypertrophy and fibrosis of myocardial tissue. These results indicate that PN@Col not only exhibits potent antioxidant and anti-ferroptosis effects at the molecular and cellular levels but also significantly enhances cardiac function in the overall animal model.

PN@Col has shown vast potential in clinical applications. Firstly, its high bioavailability and specificity make it an ideal candidate for treating HF. Secondly, PN@Col's multiple synergistic actions not only provide antioxidant effects but also regulate ferroptosis, offering a new strategy for the comprehensive treatment of HF. Furthermore, the nanoparticle structure of PN@Col enhances drug delivery systems, improving stability and efficacy in vivo. However, PN@Col also faces challenges in clinical applications, such as large-scale production and quality control, necessitating further research and optimization.

Compared to previous studies, this research demonstrates significant advantages in innovation and effectiveness. While previous strategies for antioxidant and ferroptosis regulation have partially alleviated the symptoms of HF, issues such as low bioavailability and poor targeting have been identified. In this study, the use of the PN delivery system not only greatly improved the drug's bioavailability but also enhanced the therapeutic effects through synergistic actions. Furthermore, by combining scRNA-seq analysis with in vivo and in vitro experiments, this research systematically evaluated the effectiveness and mechanism of PN@Col, providing new directions and insights for future research in HF treatment.

This study, through scRNA-seq analysis, identified CMs as key cells mediating intercellular communication in the progression of HF. It was also discovered that CM-related aging and ferroptosis may play significant roles in the pathological process of HF. Further analysis led to the identification of the key gene STAT3 associated with CM aging and ferroptosis. Building on these findings, the research successfully developed PNs using EGCG and glycine and loaded the STAT3 agonist Colivelin into them, resulting in a novel antioxidant PN named PN@Col. Through in vivo and in vitro experiments, the study comprehensively investigated the potential inhibitory effect of PN@Col in age-related HF mice. The results demonstrate that this innovative treatment strategy can inhibit ROS generation, prevent CMs from undergoing ferroptosis, and significantly improve cardiac function in age-related HF mice.

Conclusion

This study has made significant progress in improving age-related HF by developing and validating PN@Col, demonstrating its potential scientific and clinical value. From a scientific standpoint, the research not only unveiled the critical role of STAT3 in regulating CM ferroptosis and inflammatory responses but also validated the effectiveness and mechanism of PN@Col through scRNA-seq and multi-layered experiments, providing new perspectives and data support for the pathophysiological research of HF. In terms of clinical applications, PN@Col, as a novel treatment strategy, has shown tremendous potential in enhancing the long-term prognosis and quality of life for HF patients, particularly through its synergistic effects in antioxidant and ferroptosis inhibition. This offers a promising avenue for more effective and precise clinical treatment options.

Although this study has made significant progress at multiple levels, it still has some limitations. Firstly, the sample size of the study is relatively small, particularly in *vivo* experiments, which are limited to mouse models, potentially impacting the generalizability and applicability of the results. Secondly, while the in vitro and in vivo experiments demonstrate that PN@Col exhibits promising therapeutic effects, its long-term efficacy and safety have not been thoroughly validated, and further large-scale clinical trials are needed. Additionally, this study primarily focuses on the specific pathological mechanisms of HF, lacking a comprehensive exploration of other potential pathogenic factors and mechanisms. Finally, optimization of the production process of PN@Col and the drug delivery system requires further research to ensure its stability and feasibility in clinical applications.

Future research should focus on validating PN@Col in large-scale clinical trials to assess its long-term efficacy and safety, as well as exploring its applicability in different types of HF patients. Furthermore, it is essential to optimize the production process and drug delivery system of PN@Col further to enhance its stability and bioavailability, ensuring its feasibility and cost-effectiveness in clinical applications. Simultaneously, potential applications of PN@Col in other heart diseases or related pathological conditions should be investigated to expand its therapeutic scope. By combining various omics technologies and the principles of precision medicine, further elucidation of the molecular mechanisms of PN@Col in regulating CM function can provide a theoretical basis and technical support for developing more efficient treatment strategies. Through ongoing research and exploration, PN@Col holds the promise of bringing new breakthroughs and hope for the treatment of HF and other cardiovascular diseases.

Materials and methods

Ethical statement

This study strictly adhered to relevant ethical principles and regulations concerning animal experimentation. All experimental procedures were approved by the Institutional Animal Care and Use Committee of Shengjing Hospital of China Medical University (Ethical Approval Number 2024PS359K). All animals were housed and cared for in environments meeting humane standards, and experiments were conducted with efforts to minimize pain. At the conclusion of the experiments, all mice were euthanized humanely under ether anesthesia.

Downloading and preprocessing scRNA-seq data of heart tissue samples from HF patients

Data download

The GSE183852 dataset was obtained from the Gene Expression Omnibus (GEO) database (http://www.ncbi.nlm.nih.gov/geo/). This dataset includes samples from 28 non-diseased donors (Control group samples obtained post-brain death donation) and 17 individuals with Dilated (non-ischemic) cardiomyopathy (DCM) obtained from the left ventricular (LV) heart tissue specimens (HF group samples). The DCM tissues were collected from implanted left VADs in individuals or from transplanted hearts. After filtering, the expression matrix of each sample was normalized using the NormalizeData function in the "Seurat" package.

Quality control

Initially, employ the R package "DropletUtils" to assess the expression status of each cell and filter out barcodes with no cell expression. Subsequently, further filter based on the number of Unique Molecular Identifiers (UMI) in each cell, removing cells with UMI counts less than 200. Next, utilize the “scater” package to analyze gene expression in cells and filter out cells with mitochondrial gene expression exceeding 5% and ribosomal gene expression lower than 20%. Finally, perform gene-level statistics.

scRNA-seq data analysis

Principal component analysis (PCA) and batch effect removal

Initially, the top 2000 genes displaying the most significant differences between cells were selected using the “Seurat” package’s FindVariableFeatures function. Focusing on these genes in downstream analysis helps highlight biological signals within the single-cell dataset. Subsequently, the expression data was scaled linearly using the “Seurat” package’s ScaleData function, followed by linear dimensionality reduction analysis using the “Seurat” package’s RunPCA function. Finally, the “harmony” package’s RunHarmony function was employed to mitigate sample-to-sample variations.

Cell dimensionality reduction and clustering

Following batch effect correction, the principal components (PCs) with the highest standard deviation were selected first. Subsequently, cell clustering analysis was performed using the "Seurat" package's FindNeighbors and FindClusters functions. Uniform manifold approximation and projection (UMAP) was then conducted using the "Seurat" package's RunUMAP function.

Identification of marker genes

Initially, differential expression genes between each cluster and all other cells were calculated using the "Seurat" package's FindMarkers function ($|\log2FC| \geq 0.1$, minimum cell group expression ratio of 0.25, p-value ≤ 0.05), thus identifying marker genes (top 500 logFC genes).

Cell annotation

The cells were annotated based on existing marker genes, and cluster visualization was conducted. Subsequently, the proportions of different cell types in each group were calculated to determine the variance in cell type proportions among groups, aiding in the identification of core cell clusters. Using the identified core cell clusters, further dimensionality reduction clustering was performed to determine marker genes for subtyping and to calculate cell type proportions in each sample, assessing intergroup proportion differences. Subsequently, subtyping of core cell clusters (including CMs, macrophages, and T cells) was carried out using UMAP, enabling dimensionality reduction clustering analysis of single-cell data. Common markers for CM and macrophage subtypes were not identified; thus, annotation was performed using a heuristic clustering approach.

Differential analysis

The differential expression analysis of the core cell groups (HF vs Control) was conducted using the "Seurat" package's FindMarkers function. The selection criteria were set as fold change (FC) > 1.2 and p-value < 0.05.

Functional enrichment analysis

The intersecting genes were subjected to Gene Ontology (GO) enrichment analysis utilizing the "ClusterProfiler" package in R. This analysis included exploration of biological processes (BP), molecular functions (MF), and cellular components (CC), followed by the visualization of the GO enrichment results through bubble charts and gene network diagrams. A cutoff of $|\log2FC| > 1$ and P-value < 0.05 was applied for filtering. Subsequently, based on the $|\log2FC|$ values, candidate target genes underwent Kyoto Encyclopedia of Genes and Genomes (KEGG) enrichment analysis using the "ClusterProfiler" package in R, with resulting bubble charts and gene network diagrams.

Venn analysis

A set of 728 genes related to ferroptosis was obtained from the FerrDb database (http://www.zhounan.org/ferrdb/current/). Additionally, 5740 genes associated with senescence were extracted from the GeneCards database (https://www.genecards.org/) using the search term "senescence." Intersection genes were identified by conducting a Venn analysis in R using the "VennDiagram" package between the aforementioned two gene sets and the differentially expressed genes (DEGs) in CM_1 and CM_2.

AUCell scoring

In order to identify cell clusters regulated by aging, inflammation, and ferroptosis in HF, this study conducted AUCell analysis on individual cells based on gene labels associated with aging, inflammation, and ferroptosis. The differences in aging, inflammation, and ferroptosis scores between the disease group and the control group were explored using the Wilcoxon test.

Pyscenic Analysis

To investigate transcriptional factor regulatory variances among all core cells, abnormally activated transcription factors were further selected from HF samples according to grouping. SCENIC was employed to infer the regulatory activity of each transcription factor based on the expression levels within the core cell subtypes.

Cell communication analysis

Cell-to-cell communication analysis was conducted based on the specific expression genes of various cell types and ligand-receptor relationships collected from the literature. Cell interaction analysis was performed separately according to the grouping to select abnormal aging, inflammation, and related ligand-receptor axes. The "cellchat" package was utilized to infer cell-to-cell communication based on the expression values of receptor-ligand genes corresponding to various cell types, thereby constructing a network of receptor-ligand pairs between cells.

Cell culture and treatment

Human CMs (CP-H076, Wuhan Punose Life Sciences, Wuhan, China) were cultured using a human CM complete medium (CM-H076, Wuhan Punose Life Sciences, Wuhan, China). Human embryonic kidney cells HEK-293 T (Bio-72947, Beijing Bio-Bos Biological Technology Co., Ltd) were cultured in DMEM high glucose medium

(11,965,084, Thermo Fisher Scientific, USA) containing 10% FBS (10100147C, Thermo Fisher, USA) and 1% penicillin–streptomycin (100 U/mL penicillin and 100 μg/mL streptomycin, 15,140,163, Thermo Fisher, USA). The cells were maintained in a humidified incubator at 37 °C with 5% CO_2 (Heracell™ Vios 160i CR CO_2 Incubator, 51,033,770, Thermo Scientific™, Germany). Passaging was carried out when the cells reached 80% ~ 90% confluency.

Treat CM cells with 5 μM ferroptosis inducer Erastin (HY-15763, MedChemExpress, USA) to induce cell ferroptosis. After treatment for 24 h, further treat the cells with different reagents for another 24 h and conduct subsequent biochemical tests [52, 53].

Lentivirus transduction

CMs were silenced using lentivirus infection, with lentivirus packaging services provided by Shengwu Bioengineering (Shanghai, China). The pHAGE-puro plasmid series and auxiliary plasmids pSPAX2 and pMD2.G (catalog numbers #118,692, #12,260, and #12,259, respectively, purchased from Addgene, USA) were utilized for gene overexpression. For gene silencing, the pSuper-retro-puro plasmid series and auxiliary plasmids gag/pol and VSVG (catalog numbers #113,535, #14,887, and #8454, respectively, obtained from Addgene, USA) were employed. The aforementioned plasmids were co-transfected with lentivirus packaging, facilitated by Shengwu Bioengineering. The constructed plasmids were co-transfected into HEK293T cells using Lipofectamine 2000 reagent (11,668,030, Thermo Fisher, USA), followed by harvesting the supernatant after 48 h of cell culture. The supernatant, post-centrifugation using a 0.45 μm filter, was collected as the virus, which was concentrated after 72 h by centrifugation of the supernatant. The two virus preparations were mixed, and viral titer was determined.

During the logarithmic growth phase, cells were digested with trypsin and seeded at a density of 1×10^5 cells per well in a 6-well plate. Following 24 h of routine culture, when cell confluency reached approximately 75%, the cells were infected with lentivirus packaging at a multiplicity of infection (MOI) of 10 and a working titer of about 5×10^6 TU/mL, supplemented with 5 μg/mL polybrene (TR-1003, Merck, USA) in the medium. After 4 h of infection, an equal volume of medium was added to dilute the polybrene, and 24 h post-infection, the fresh medium was replaced. For the establishment of stable cell lines, cells were further cultured in a medium containing 2 μg/mL puromycin (E607054, Shengwu Bioengineering, Shanghai, China). During passaging, the puromycin concentration was gradually increased in a stepwise manner at 2, 4, 6, 8, and 10 μg/mL to perform resistance screening and obtain stable transduced cell lines. Cells were collected once they no longer exhibited cell death in the presence of a puromycin-containing medium. The efficiency of knockout was confirmed through Western blot and RT-qPCR analyses. Lentivirus sequences for silencing are detailed in Table S3, with subsequent selection of the most effective silencing sequence for experimental validation [54].

Cell groups were categorized as follows: sh-NC CMs (control cells with lentivirus silencing STAT3); sh-STAT3 CMs (cells with silenced STAT3); oe-NC CMs (control cells with lentivirus overexpressing STAT3); and oe-STAT3 CMs (cells overexpressing STAT3).

Detection of gene expression by RT-qPCR

After one week of HF model construction or at the end of treatment, mice were euthanized, and total RNA from tissues and cells was extracted using the Trizol reagent kit (A33254, Thermo Fisher, USA). The extracted RNA was reverse transcribed using the reverse transcription kit (RR047A, Takara, Japan) to obtain the corresponding cDNA. The reaction system was prepared using the SYBR® Premix Ex TaqTM II kit (DRR081, Takara, Japan), and the samples were subjected to RT-qPCR using a real-time fluorescence quantitative PCR instrument (ABI7500, Thermo Fisher, USA). The PCR program was designed as follows: an initial denaturation at 95 ℃ for 30 s, followed by cycling with denaturation at 95 ℃ for 5 s, annealing at 60 ℃ for 30 s for 40 cycles, final extension at 95 ℃ for 15 s, extension at 60 ℃ for 60 s, and a further extension at 90 ℃ for 15 s to generate amplification curves. GAPDH was used as an internal reference, with three replicates for each RT-qPCR setting, and the experiment was repeated three times. The expression ratio of the target gene in the experimental group compared to the control group was calculated using the $2^{-\Delta\Delta CT}$ method, where $\Delta\Delta CT = \Delta Ct_{\text{experimental group}} - \Delta Ct_{\text{control group}}$, and $\Delta Ct = Ct_{\text{target gene}} - Ct_{\text{internal reference gene}}$. Ct represents the cycle threshold when the real-time fluorescence intensity reaches the set threshold, indicating logarithmic growth of amplification. The primer details are provided in Table S4.

Western blot analysis

Total proteins from tissues and cells were extracted using RIPA (Radio Immunoprecipitation Assay) lysis buffer (P0013B, Beyotime, Shanghai, China) containing 1% PMSF (Phenylmethanesulfonyl fluoride) following the manufacturer's instructions. The protein concentration of each sample was determined using a BCA protein assay kit (P0011, Beyotime, Shanghai, China) on the supernatant, and protein concentrations were adjusted to 1 μg/μL. Each sample was then boiled at 100 ℃ for 10 min to denature the proteins and stored at – 80 ℃ for

later use. SDS-PAGE gels (8–12%) were prepared based on the expected size of the target protein bands, and 50 μg of protein samples were loaded into each lane using a micropipette. The gel was electrophoresed at a constant voltage of 80 V to 120 V for 2 h. Transblotting was performed at a constant current of 250 mA for 90 min to transfer the proteins from the gel to a PVDF membrane (1,620,177, Bio-Rad, USA).

The membrane was blocked with 1 × TBST containing 5% non-fat milk at room temperature for 1 h. The blocking solution was then discarded, and the membrane was washed with 1 × TBST for 10 min. Primary antibodies (antibody details in Table S5) were incubated overnight at 4 ℃, followed by three washes with 1 × TBST for 10 min each at room temperature. Subsequently, the membrane was washed three times with 1 × TBST for 5 min each at room temperature. The membrane was then incubated with HRP-conjugated goat anti-rabbit IgG (ab6721, dilution 1:5000, Abcam, Cambridge, UK) or goat anti-mouse IgG (ab205719, dilution 1:5000, Abcam, Cambridge, UK) secondary antibodies at room temperature for 1 h. After three washes with 1 × TBST buffer at room temperature for 5 min each, the membrane was immersed in ECL reaction solution (1,705,062, Bio-Rad, USA) and incubated at room temperature for 1 min. The liquid was removed, the membrane was covered with plastic wrap, and band exposure imaging was performed on the Image Quant LAS 4000C gel imaging system (GE Healthcare, USA). The relative expression levels of proteins were determined by comparing the grayscale values of the target bands to the reference bands (GAPDH as internal control), reflecting the relative protein expression levels. Protein expression levels were assessed with three replicates for each experiment.

CCK-8 proliferation assay

CMs were digested and re-suspended, and the cell concentration was adjusted to 1×10^5 cells/mL before seeding 100 μL per well into a 96-well plate for overnight incubation. Following the manufacturer's instructions for the CCK-8 assay kit (C0041, Beyotime, Shanghai, China), cell viability was assessed using the CCK-8 method at 12, 24, 36, and 48 h post-culturing. At each time point, 10 μL of the CCK-8 detection solution was added, and the plate was then placed in a 37 °C, 5% CO_2 incubator for 2 h. The absorbance at 450 nm was measured using a microplate reader (BioTek, USA) to calculate cell viability according to the following formula [55].

$$Cellviability(\%) = \left(\frac{OD_{sample} - OD_{blank}}{OD_{control} - OD_{blank}} \right) \times 100$$

OD_{sample} represents the optical density value of the drug-treated samples. $OD_{control}$ refers to the optical density value of the control group (untreated cells under normal growth conditions). OD_{blank} denotes the optical density value of the blank control (comprising culture medium and CCK-8 reagent, but without cells).

EDU staining

CMs were seeded in a 24-well plate with a density of 1×10^5 cells per well. Each group of cells was triplicated. 5-Ethynyl-2'-deoxyuridine (EdU) solution (ST067, Beyotime, Shanghai, China) was added to the culture medium to achieve a concentration of 10 μmol/L, followed by 2 h of incubation in a CO_2 incubator. After removal of the culture medium, cells were fixed at room temperature for 15 min in PBS solution containing 4% paraformaldehyde, washed twice with PBS containing 3% BSA, permeabilized with 0.5% Triton-100 in PBS at room temperature for 20 min, washed again with PBS containing 3% BSA, and incubated with 100 μL of staining solution per well at room temperature in the dark for 30 min. Cell nuclei were stained with DAPI (C1002, Beyotime, Shanghai) for 5 min. The coverslip was then examined under a fluorescence microscope (Model: FM-600, Shanghai Pudan Optical Instrument Co., Ltd) to observe 6–10 random fields per well and record the number of positive cells in each field. The EdU labeling rate was calculated as the percentage of positive cells out of the total cells (positive cells + negative cells) × 100% [55]. Each experiment was repeated three times.

Transwell migration assay

To assess the migration capability of CMs, Transwell inserts with a pore size of 8 μm on polycarbonate membranes (3428, Corning, USA) were used. The lower chambers were pre-filled with 600 μL of culture medium containing 20% FBS and incubated at 37 °C for 1 h. After treating the cells, they were resuspended in an FBS-free medium, seeded at a concentration of 1×10^6 cells/mL in the upper chambers, and incubated at 37 °C with 5% CO_2 for 24 h. The Transwell inserts were then removed, washed twice with PBS, fixed with 5% glutaraldehyde, stained with 0.1% crystal violet at 4 °C for 5 min, washed again with PBS, and surface cells were removed using a cotton ball. The cells were observed under a light microscope, and images were taken of 5 random fields. The average number of cells that migrated across the insert was calculated for each group. Each experiment was repeated three times [55].

Wound healing assay

On the bottom of a 6-well plate, lines were marked at 0.5–1 cm intervals using a ruler and marker, with each well crossed by at least 5 lines. CMs were seeded into the wells at a density of 5×10^5 cells per well. When cells

reached 100% confluence, a 200 μL pipette tip was used to create a scratch perpendicular to the marked lines on the back. Suspended cells were washed off with sterile PBS and replaced with a complete medium containing 2% serum. The scratches were observed at 0 h and 24 h under an optical microscope (model: DM500, Leica) to measure the gap distance between the wound edges. Images were captured under an inverted microscope to assess cell migration in each group. The distance between the scratches was analyzed using Image-Pro Plus 6.0 software, and the wound healing rate was calculated using the following formula [55].

$$Woundhealingrate = \frac{distance_{0h} - distance_{24h}}{distance_{0h}}$$

Here, $distance_{0\,h}$ and $distance_{24\,h}$ represent the gap distance between the cells at 0 h and 24 h after scratching, respectively.

Flow cytometry analysis

The apoptosis level of CMs was assessed using the Annexin V-FITC/PI assay kit (C1062L, Beyotime, Shanghai, China). Cells were seeded in 6-well plates, with 1×10^6 cells per well. Following cell collection, 195 μL of Annexin V-FITC binding buffer was added to resuspend the cells. Subsequently, 5 μL of Annexin V/FITC solution and 10 μL of PI solution were added, followed by a 15 min incubation at room temperature in the dark. Flow cytometry analysis was conducted within 20 min to determine the percentage of apoptotic cells. The apoptosis rate was calculated as the sum of apoptotic cells in the Q1-UR (upper right) and Q1-LR (lower right) quadrants [55].

Detection of Fe2 + Ions

The FerroOrange probe (F374, Dojindo, Japan) was used to assess the levels of Fe^{2+} ions inside the cells. Pretreated CMs were seeded on confocal culture dishes, washed with Hank's balanced salt solution (HBSS; 13,150,016, Gibco), and then incubated with 1 μM FerroOrange for 30 min. The cells were observed under a confocal laser scanning microscope (LSM780, Zeiss). Simultaneously, the iron content in cells and tissues was determined using an iron content detection kit (MAK025, Sigma-Aldrich). For tissue samples, homogenization was conducted by adding 1 mL of distilled water, followed by centrifugation to obtain the supernatant. Cell samples were collected and centrifuged directly to obtain the supernatant. Subsequently, 100 μL of the supernatant from each well was transferred to a flat-bottom 96-well UV detection plate. A mixture of 35 μL of reagent, 5 μL of reagent B, and 150 μL of reagent C was thoroughly combined with the samples, followed by a 5 min incubation at room temperature. The absorbance was read at 359 nm using an Epoch microplate spectrophotometer. The Fe^{2+} content was normalized to the protein concentration. Each experiment was repeated three times.

TEM

CMs and heart tissue were prepared for TEM. The samples were fixed overnight at 4 °C in a 2.5% glutaraldehyde solution (P1126, Beijing Solabao Technology Co., Ltd., Beijing, China), followed by fixation in a 1% osmium tetroxide solution (115,355, ECHO Chemicals, Chengdu, China) for 1–2 h at room temperature. Dehydration was carried out in graded ethanol (50%, 70%, 80%, 90%, and 95%), followed by treatment with pure acetone and overnight incubation in pure embedding resin. The samples were then embedded after infiltration and heated overnight at 70 °C to complete embedding. Thin sections of 70–90 nm thickness were obtained using a Reichert ultramicrotome. These sections were stained with lead citrate and 50% ethanol-saturated uranyl acetate for 15 min each, enabling observation under TEM.

Measurement of mitochondrial membrane potential

Cells were seeded into a 6-well culture plate using the JC-1 mitochondrial membrane potential assay kit (40706ES60, Yisheng Biotechnology, Shanghai, China), with 1 mL of JC-1 staining working solution added to each well and thoroughly mixed. The cells were then incubated at 37 °C for 20 min in a cell culture incubator. CCCP provided in the kit (50 mM) was added to the cell culture medium at a 1:1000 ratio, diluted to 50 μM, and the cells were treated for 20 min as a positive control. After the incubation at 37 °C, the supernatant was removed, and the cells were washed twice with JC-1 staining buffer (1×). Subsequently, 2 mL of cell culture medium containing serum and phenol red was added. The observation was conducted under a fluorescent microscope or a confocal laser scanning microscope, with the excitation light set at 490 nm and emission light at 530 nm to detect JC-1 monomers.

Biochemical analysis

The levels of reduced glutathione (GSH) and oxidized glutathione (GSSG) within cells and tissues were determined using the GSH and GSSG assay kit (S0053, Beyotime) following the manufacturer's instructions. The absorbance of samples was measured at 450 nm using a microplate reader (E8051, Promega), and quantification was performed using a standard curve.

To detect the malondialdehyde (MDA) content, the MDA assay kit (BC0025, Solarbio) manufacturer's instructions were followed. For MDA detection, the supernatant of cell homogenates and the prepared

working reagent were transferred to a 96-well plate. The absorbance was measured at 600 nm, 532 nm, and 450 nm using an automated microplate reader (Infinite200, Tecan, Beijing) for further calculations.

Cells grown on confocal culture dishes were stained with 5 μM C11-BODIPY581/591 (D3861, Thermo Fisher, USA) in the dark for 15 min and observed under a fluorescent microscope. The fluorescence properties change from red to green when oxidized by free radicals.

Detection of ROS

ROS levels were measured using a ROS detection kit (S0033S, Beyotime, Shanghai). DCFH-DA was diluted 1:1000 in serum-free medium to a final concentration of 10 μM/L, and cells were incubated at 37 °C for 20 min. After washing three times with serum-free medium, fluorescence intensity was observed using a fluorescence microscope (FV-1000/ES, Olympus, Japan) and analyzed with Image J. Each experiment was repeated three times.

For tissue ROS measurement, a tissue ROS detection kit (HR8821, Biovision) was used. Tissue samples (50 mg) were homogenized, centrifuged at 100×g for 3 min at 4 °C, and the supernatant collected. A mixture of 200 μL supernatant and 2 μL DHE probe was incubated in a 96-well plate at 37 °C in the dark for 15–30 min. Fluorescence intensity was measured at an excitation wavelength of 488–535 nm and an emission wavelength of 610 nm using a microplate reader (E8051, Promega). Tissue ROS levels were expressed as fluorescence intensity (RFU) per mg of protein. Each experiment was performed in triplicate.

Preparation of novel antioxidant PNs

Sixty-one milligrams of EGCG (HY-13653, MedChemExpress, USA) were dissolved in a 5% ethanol solution containing 10 μL of formaldehyde and 37% triethylamine (TEA, T0886, Sigma-Aldrich, USA) in 40 mL and vigorously stirred for dissolution at 30 ℃. Subsequently, 10 mg of glycine (Gly, HY-Y0966, MedChemExpress, USA) was added to the solution, and the reaction was continuously stirred for 48 h. The nanoparticles were obtained by centrifugation at 10,000 r/min-1 for 10 min to yield PNs, which were then purified by washing three times with 10 mL of water and resuspended in 5 mL of water for storage at 4 ℃.

To dissolve the PNs, 2 mg of the nanoparticles were mixed with 100 μL of ethanol. Subsequently, 2 mg of the STAT3 agonist Colivelin (referred to as Col, HY-P1061, MedChemExpress, USA) was added to the mixture and vigorously stirred at 30 ℃. The nanoparticles were then reassembled in a deionized water and ethanol solution. After centrifugation at 10,000 r/min^{-1} for 10 min, the nanoparticles were washed three times with 10 mL of water, followed by freeze-drying to obtain PN@Col.

Morphology, size, and distribution of nanoparticles

The size and shape of nanoparticles were observed using TEM. Prior to scanning, 20 μL of freshly prepared nanoparticle samples in suspension were loaded onto carbon-coated copper electron microscopy grids. Negative staining was performed using 1% uranyl acetate (CD106833, Guangzhou Wei Pharmaceuticals Technology Co., Ltd., Guangzhou, China) for 5 min. This method provided high-quality contrast and sharpness for clear and distinct visualization of the samples. Subsequently, the grids were washed thrice with PBS, the excess phosphotungstic acid solution was removed using filter paper, and the grids were left semi-dried. The images were observed at 100 kV using a Hitachi H7650 TEM (Hitachi, Japan).

The scanning electron microscopy (SEM) procedure for detecting lipid nanoparticles involves the following steps: Lipid nanoparticles were examined using a scanning electron microscope (S-4800, Hitachi, Japan) under an accelerating voltage of 3 kV. The sample was loaded onto a conductive adhesive tape mounted on the SEM sample stub and coated with a thin layer of gold using a sputter coater (Cressington Scientific Instruments, Watford, UK) for 60 s before observation with SEM.

Nanoparticle Tracking Analysis (NTA): 20 μg of nanoparticles were dissolved in 1 mL of PBS and vortexed for 1 min to ensure uniform dispersion of LNP@Ket. The nanoparticle size distribution was directly observed and measured using a ZetaView Nanoparticle Tracking Analyzer (Particle Metrix, Germany) through dynamic light scattering (DLS). The average size of the exosomes and the Polymer Dispersity Index (PDI) were determined, and the Zeta potential value of the exosomes was measured by conducting three measurements for each sample.

PN@Col drug loading and encapsulation efficiency test

Freeze-dried PN@Col was accurately weighed, dissolved in a 50:50 mixture of acetonitrile (AcN, Thermo Fisher) and water, and analyzed by HPLC (Ascentis C18 column, 25 cm×4.6 mm, 5 μm, Agilent). The mobile phase was AcN:water (50:50) at a flow rate of 1 mL/min. Colivelin was detected at 227 nm using a UV detector. Drug loading was calculated as the weight percentage of Colivelin in PN@Col, and encapsulation efficiency was determined based on its weight [56].

PN@Col in vivo *and* in vitro *drug release testing*

For the release kinetics study, in vitro, the PN@Col containing Colivelin was suspended in 1 mL of PBS (Procell, PB180327, China) containing 0.1% Tween 80 (Sigma,

P1754-1L, USA) and incubated in a rotating shaker at 37 °C. At regular time points, the PN@Col suspension was centrifuged at 10,000 rpm for 10 min, and 0.9 mL of the supernatant was collected and replaced with fresh buffer. After the final collection at 72 h, the remaining PN@Col was freeze-dried and dissolved in a 50:50 mixture of AcN and water. The released samples and remaining PN@Col were analyzed by HPLC [56].

Assessment of antioxidant capacity

Antioxidant activity was evaluated using DPPH and ABTS free radical scavenging assays.

For the DPPH assay, varying concentrations of nanoparticles were added to a freshly prepared 0.4 mM DPPH methanol solution and incubated at 25 °C for 30 min under subdued light. Absorbance was measured at 517 nm using a UV–visible spectrophotometer (TU-1901, Persee, China).

For the ABTS assay, ABTS stock solution was prepared by mixing 7 mM ABTS (5 mL) with 140 mM potassium persulfate (88 µL) and incubating in the dark for 10–16 h. The stock was diluted 20-fold with 80% methanol to adjust the absorbance to 0.75 ± 0.05 at 734 nm. In a 96-well plate, 100 µL of the methanol nanoparticle solution at varying concentrations and 100 µL ABTS working solution were mixed and incubated at 25 °C in the dark for 30 min. Absorbance was measured at 734 nm using a microplate reader. The scavenging activity was calculated using:

$$Y = \left(1 - \frac{A_{sample} - A_{control}}{A_0}\right) \times 100\%$$

A_{sample} is the absorbance of DPPH or ABTS solutions after adding nanoparticles, $A_{control}$ represents the absorbance of DPPH or ABTS solutions without samples, and A_0 indicates the absorbance of DPPH or ABTS solutions lacking antioxidants.

The antioxidant capacity was compared using Trolox (HY-101445, MedChemExpress, USA) as a reference. The equivalent antioxidant capacity (TEAC) was calculated as:

$$\frac{EC_{50}(Trolox)}{250.34} \times \frac{1}{EC_{50}(sample)} \times 1000 = Antioxidantcapacity(mmolTEg^{-1}).$$

Where 250.34 represents the molecular weight of Trolox. EC_{50} is the concentration of the sample found in the linear relationship that inhibits 50% of free radicals.

Detection of live cell density

CMs were seeded in a 12-well plate at a density of 1×10^5 cells per well, with each group of cells having three replicate wells. After incubating for 12 h to allow cell adhesion, the cells were treated with either PN or PN@Col for another 12 h. Subsequently, live cells were labeled with fluorescein diacetate (FDA, F1303, Thermo Fisher, USA) and observed under a fluorescence microscope for image analysis. The percentage of viable cells was calculated based on the proportion of fluorescent cells.

Establishment of an aged mouse model of HF

Aged SPF C57BL/6 mice over 24 months of age (219, Beijing Vital River Laboratory Animal Technology Co., Ltd., Beijing, China), weighing 18–25 g, were housed in SPF animal facilities with controlled lighting of 12 h light/12 h dark, humidity maintained at 60–65%, and temperature between 22 and 25 °C. The mice were provided ad libitum access to food and water and acclimated for 1 week before the experiment, during which their health status was monitored. The experimental procedures and animal protocols were approved by the Institutional Animal Care and Use Committee.

Mice were anesthetized with 2% isoflurane in 100% O_2 (1 L/min) and intubated using a 20G catheter. Ventilation was maintained via a respirator (MiniVent Model 845, Harvard Apparatus) delivering 2% isoflurane in oxygen at 1 L/min, with a tidal volume of 150 µL and a respiratory rate of 150 bpm. After hair removal and disinfection (iodine and 70% alcohol, three times), a midline incision was made from the manubrium to the xiphoid process. A partial sternotomy was performed to expose the aortic arch using a rib spreader. Adipose tissue was cleared, and a titanium micro-clip was placed, reducing the aortic arch cross-section by ~ 50%.

The rib spreader was removed, and the ventilator's expiratory circuit was briefly occluded (2–3 s) to induce heart overinflation, increasing the tidal volume to 200 µL. The thoracic wall and skin were sutured, tidal volume was reset to 150 µL, and isoflurane was gradually reduced to 0.5% until spontaneous respiration resumed. The endotracheal tube was removed, and mice recovered in a heated cage for 30 min to 1 h. Sham-operated mice underwent the same procedure without micro-clip placement. All mice were maintained for 8 weeks before CO_2 euthanasia and further interventions.

Mice were randomly divided into five groups (n = 6 per group). Three days post-HF model construction, treatments were administered via daily tail vein injections for 28 days: Sham group: Thoracotomy without aortic manipulation, received 100 µL PBS; PNs group: 100 µL PNs (equivalent to 2 mg/kg colivelin) in PBS; Model group: HF mice received 100 µL PBS; Colivelin group: 100 µL PBS with 2 mg/kg colivelin; PN@Col group: 100 µL PBS with 2 mg/kg PN@Col.

Cardiac function was assessed every 7 days. After 28 days, mice were euthanized for biochemical analysis of cardiac tissues [37, 53, 57].

Echocardiographic examination Protocol

Echocardiographic examinations were performed using the Visual Sonics Vevo 2100 system (Visualsonics Inc., Toronto, Canada) equipped with a 21 MHz linear array transducer. The procedure was conducted as follows. Mice were positioned supine on a heated platform under continuous anesthesia with 2% isoflurane gas. The chest fur was shaved using an electric shaver and then depilated with hair removal cream. Parasternal long-axis (PLAX) and short-axis views were obtained. In the PLAX view at the level of the aortic sinus, measurements were taken of the left ventricular posterior wall thickness (LVPWT), interventricular septum thickness (IVST), left ventricular end-diastolic dimension (LVEDD), left ventricular end-systolic dimension (LVESD), left ventricular ejection fraction (LVEF), and left ventricular fractional shortening (LVFS) [58, 59].

ELISA for inflammatory cytokines

Inflammatory cytokines TNF-α (Abcam, #ab252354), IL-1β (Cloud-clone, #SEA563Si96T), and IFN-γ (Chenglin, #AD0081Mk) were measured using ELISA kits following the manufacturer's instructions. Required microplates were prepared, with unused plates stored at 4 °C. Reagents were brought to room temperature for 20 min before use.

Standards and samples were diluted as instructed, and 10 µL of each was added to wells, sealed, and incubated at 37 °C for 90 min. Wells were washed four times, then incubated with biotinylated antibodies at 37 °C for 60 min, followed by enzyme-conjugated solution for 30 min. After washing, 100 µL of chromogenic substrate was added and incubated in the dark at 37 °C for 10–20 min. The reaction was stopped with 100 µL of stop solution, and absorbance was measured at 450 nm [60].

Hemodynamic parameter assessment in mice

Mice were positioned supine and secured on the surgical table under continuous anesthesia with 2% isoflurane gas. A multi-channel physiological signal acquisition system (MP150, BIOPAC, USA) was utilized to measure left ventricular systolic pressure (LVSP), left ventricular end-diastolic pressure (LVEDP), maximum rate of rise of left ventricular pressure (+dp/dt), and maximum rate of fall of left ventricular pressure (− dp/dt) [58, 59].

Hematoxylin and eosin (H&E) staining

H&E staining was performed on cardiac tissue to observe pathological changes using a H&E staining kit (C0105S, Beyotime, Shanghai, China). Following the completion of treatment, mice were euthanized, and sections of the the heart, kidney, and liver tissues were fixed in 4% paraformaldehyde (P0099, Beyotime, Shanghai, China), dehydrated, cleared, and embedded in paraffin. Thin sections of 5 µm were prepared using a microtome, followed by baking, deparaffinization, hydration to water, staining with hematoxylin, rinsing with distilled water, immersion in 95% ethanol, eosin staining, differentiation with 70% hydrochloric acid ethanol, dehydration, clearing, and mounting with neutral resin. The slide preparation was then examined under an optical microscope to assess the morphological changes in the mouse cardiac tissue [53].

Masson staining

A Masson trichrome staining kit (DC0032, Leagene Biotechnology, Beijing, China) was utilized to assess the level of atrial fibrosis in the tissue sections. After dewaxing 4 µm thick sections in water, the slides were stained with hematoxylin for 5–10 min, differentiated in acidic alcohol for 5–15 s, rinsed in water, and then immersed in Masson's blue solution for 3–5 min. Subsequently, after another water rinse, slides were stained with Ponceau S for 5–10 min, washed in phosphomolybdic acid solution for 1–2 min, counterstained with aniline blue solution for 1–2 min, dehydrated in ethanol, cleared in xylene, and finally mounted for observation. Images were captured at 200× magnification using an Olympus BX51 microscope (Tokyo, Japan) and analyzed with ImagePro Plus 6.0 imaging software. Three random slices were taken from each mouse, from apex to base of the heart, with 5 fields of view observed on each slide under high magnification, in accordance with a single-blind protocol. The collagen volume fraction (CVF) was quantified by measuring the ratio of the blue-stained area to the total atrial area.

Sirius red staining

Following the completion of the treatment, mice were euthanized, and 6 µm thick sections of mouse heart tissue were dewaxed in water. The sections were then stained with hematoxylin for 10–20 min, differentiated in acid differentiation solution for 10 s, rinsed in running water for 10 min, and subsequently stained with Sirius Red dye (365,548-5G, Sigma-Aldrich, USA) for 1 h at room temperature. After a water rinse, the slides were dehydrated, cleared, and finally mounted for observation. Three random slices were taken from each mouse, with 5 fields of view observed on each slide under high magnification. The ImagePro Plus 6.0 software was utilized to perform a semi-quantitative analysis of the Picro Sirius Red-positive area.

Wheat germ agglutinin (WGA) staining

After fixing mouse heart tissues in 4% paraformaldehyde for 24 h, the tissues underwent dehydration using a series of ethanol concentrations, followed by clearing in xylene and embedding in paraffin. Subsequently, tissue sections were stained with WGA staining solution (W11261, Thermo Fisher, USA), which binds specifically to sugars on the cell membrane. The slides were then mounted with a neutral mounting medium to complete the slide preparation. Following staining, the samples were observed under a fluorescence microscope to analyze the cellular structure and changes in the heart tissue.

Immunohistochemical staining

Paraffin-embedded tissue sections were air-dried overnight, baked at 60 °C for 20 min, deparaffinized in xylene (2×10 min), and rehydrated through graded ethanol to distilled water. Antigen retrieval was performed in citrate buffer (pH 6.0) using a microwave (8 min), followed by cooling to room temperature. Sections were washed with PBS (3×3 min), treated with 3% H_2O_2 for 10 min, and blocked with goat serum (20 min, room temperature).

Sections were incubated overnight at 4 °C with rabbit anti-p-STAT3 antibody (ab76315, 1:100, Abcam), washed, then incubated with goat anti-rabbit IgG (ab6721, 1:5000, Abcam) for 30 min, followed by Streptavidin–Biotin Complex (SABC, P0603, Beyotime) at 37 °C for 30 min. Staining was developed using a DAB kit (P0203, Beyotime) for 6 min, and counterstained with hematoxylin (30 s).

Sections were dehydrated through graded ethanol, cleared in xylene (2×5 min), sealed with neutral resin, and examined under a brightfield microscope (BX63, Olympus). Five high-power fields per slide were analyzed using Image-Pro Plus 6.0, with experiments repeated three times.

Detection of apoptosis in cells using TUNEL assay

Mouse heart tissues were fixed in 4% paraformaldehyde for 15 min, washed with PBS three times, and permeabilized in 0.1% Triton-X 100 in PBS for 3 min. Subsequently, the cardiac tissues were stained using the TUNEL assay kit (C1090, Beyotime, Shanghai, China) to detect apoptosis. This process involved incubating the samples with 50 μL of biotin-labeled solution at 37 °C in the dark for 60 min, followed by three washes with PBS. Then, 0.3 mL of the labeling reaction termination solution was added, followed by three more washes with PBS. Next, 50 μL of Streptavidin-HRP working solution was applied to the samples and left to incubate at room temperature for 30 min, followed by another three washes with PBS. The samples were incubated with 0.5 mL of DAB chromogen at room temperature for 5 min, followed by three washes with PBS. Subsequently, the samples were counterstained with DAPI (10 μg/mL) for 10 min. The cell apoptosis ratio for each group was then calculated using the Image Pro Plus 6.0 software after observing the images of different groups under a confocal microscope.

Prussian blue staining for iron accumulation assessment in tissues

The Solarbio iron staining kit (Prussian blue staining, G1424, Solarbio Science & Technology, Beijing, China) was utilized to determine iron accumulation in tissues. Initially, mouse heart tissues were excised and fixed in 4% paraformaldehyde. Following fixation, the tissues underwent dehydration, clearing, embedding in paraffin, and sectioning into 5 μm thick slices. The slices were deparaffinized to water after baking at 60 °C, followed by staining with the Prussian blue staining reagent to detect iron ions in the tissues. Post-staining, the slices were rinsed with distilled water, underwent rapid clearing, and were finally seal-mounted using a neutral mounting medium. The stained tissue sections were observed under an optical microscope, and analysis was performed using Olyvia software to assess the accumulation of iron ions in the tissues.

Statistical analysis

The data were derived from at least three independent experiments, presented as mean ± standard deviation (Mean ± SD). For comparisons between the two groups, a two-sample independent t-test was employed. Regarding comparisons among three or more groups, a one-way analysis of variance (ANOVA) was utilized. In cases where the ANOVA results indicated significant differences, Tukey's Honestly Significant Difference (HSD) post-hoc test was conducted to compare differences between each group. For non-normally distributed or inhomogeneous variance data, the Mann–Whitney U test or Kruskal–Wallis H test is applied. All statistical analyses were performed using GraphPad Prism 9 (GraphPad Software, Inc.) and the R programming language. A significance level of 0.05 was set for all tests, with a two-tailed p-value less than 0.05 considered statistically significant.

Abbreviations

HF	Heart failure
ACE	Angiotensin-converting enzyme
VADs	Ventricular assist devices
CRT	Cardiac resynchronization therapy
ROS	Reactive oxygen species

Supplementary Information

The online version contains supplementary material available at https://doi.org/10.1186/s12951-025-03317-x.

Supplementary material 1. Fig. S1. Quality Control, Filtering, and PCA of scRNA-seq Data. Note: (A) Cell expression plot showing the relationship between the total gene expression counts per single cell (x-axis) and the number of genes detected (y-axis) in each cell; (B) Histograms on the upper left display the distribution of gene expression levels in single cells, while the ones on the upper right show the average intensity of gene expression in each sample. The two plots at the bottom illustrate the impact of different gene detection thresholds on intra-sample cells, determining the gene expression threshold used for subsequent analysis; (C) Proportional relationship between different gene expression levels and total cell counts to assess dominant genes in the dataset and their expression uniformity within samples; (D) PCA results of the top 15 highly and lowly expressed genes in the top 2 PCs; (E) Heat map showing the top 20 predominantly associated gene expressions with PC_1 to PC_7 in PCA, where yellow indicates upregulation and purple indicates downregulation of gene expression; (F) Sample distribution revealed by PCA, indicating potential groupings or patterns between samples with different colors and markers; (G) Distribution of standard deviations of PCs, with important PCs having larger standard deviations, and the red line represents the screening threshold; (H) Distribution of cells after Harmony batch correction, each point representing a cell, where red points denote Control group samples (n=28) and blue points represent HF group samples (n=17); (I) Distribution of cell features after Harmony batch correction, with features values gradually increasing from blue to orange. Fig. S2. Cell Clustering Analysis of scRNA-seq Data. Note: (A) UMAP visualization of cell clustering results, where each branch on the dendrogram represents a unique cluster of cells, aiding in the identification and interpretation of different cell types or states; (B) Group visualization of UMAP clustering results, illustrating the aggregation and distribution of cells from different source samples, with each point representing a cell and different colors indicating distinct clusters; (C) UMAP clustering results displaying the aggregation and distribution of cells from different source samples, with each point representing a cell, and different colors indicating distinct clusters, where the left plot represents the Control group (n=28) and the right plot represents the HF group (n=17); (D) Bar graph comparing the cell numbers in each cell cluster, with red representing the Control group (n=28) and blue representing the HF group (n=17); (E) Box plot showing the changes in cell cluster proportions, with red representing the Control group (n=28) and blue representing the HF group (n=17), where * indicates comparison with the Control group, *p <0.05, **p <0.01, ***p <0.001, ****p <0.0001. Fig. S3. Expression of Marker Genes in Various Cell Clusters. Note: (A) Expression patterns of the top 10 marker genes in each of the 30 cell clusters, where each row represents a gene and each column represents a cell cluster. The color gradient (from purple to yellow) indicates variations in gene expression levels, where yellow signifies high expression and purple signifies low expression. The color bar at the top of each cell cluster denotes their assignment; (B) Distribution plot showing the expression levels of the most significant marker genes across the 30 cell clusters, with darker blue indicating higher average expression levels. Fig. S4. Expression Distribution of Marker Genes in Various Cell Subtypes. Note: (A) Distribution of CM cell marker gene expressions; (B) Distribution of pericyte cell marker gene expressions; (C) Distribution of endothelial cell marker gene expressions; (D) Distribution of macrophage cell marker gene expressions; (E) Distribution of epicardial cell marker gene expressions; (F) Distribution of mast cells marker gene expressions; (G) Distribution of endocardial cell marker gene expressions; (H) Distribution of fibroblast cell marker gene expressions; (I) Distribution of T cells marker gene expressions; (J) Distribution of adipocytes marker gene expressions; (K) Distribution of lymphatics cell marker gene expressions; (L) Distribution of neuronal cells marker gene expressions. Darker shades of blue in the figures indicate higher average expression levels. Fig. S5. Distribution of Marker Gene Expressions. Note: (A) Violin plot showing the expression of marker genes used for cell identification in different cell types, with each color representing a distinct cell type; (B) Violin plot showing the expression of marker genes used for cell identification in different cell clusters, with each color representing a cluster. Fig. S6. Analysis of Distribution and Expression Characteristics of CM Subtypes. Note: (A) UMAP distribution of CM cells in all samples, with different colors representing different samples; (B) Distribution of CM cells in Control group (n=28) and HF group (n=17), with red representing Control group (n=28) and blue representing HF group (n=17); (C) Visualization of UMAP clustering results, reclassifying CMs into two cell clusters, with different colors indicating different cell clusters; (D) Expression status of marker genes in each cell cluster; (E) Classification of CMs into CM_1 and CM_2 cells based on marker genes; (F) UMAP clustering results showing the cell distribution of CM_1 and CM_2, with different colors indicating different subtypes of CMs; (G) Heatmap of the top 10 genes expressed in CM_1 and CM_2; (H) Expression patterns of selected cell-specific marker genes in different cell subtypes, with darker blue indicating higher average expression levels and larger circles representing more cells expressing the gene; (I) Expression distribution of marker genes for different CM subtypes; (J) Proportions of CM_1 and CM_2 cells in each sample; (K) Bar chart comparing the cell numbers of different CM subtypes, with red representing Control group (n=28) and blue representing HF group (n=17); (L) Box plot showing the changes in proportions of CM subtypes, with red representing Control group (n=28) and blue representing HF group (n=17), * indicates significance compared to Control group, **p <0.01.Fig. S7. Analysis of Distribution and Expression Characteristics of Macrophage Subtypes. Note: (A) UMAP distribution of Macrophage cells in all samples, with different colors representing different samples; (B) Distribution of Macrophage cells in Control group (n=28) and HF group (n=17), with red representing Control group (n=28) and blue representing HF group (n=17); (C) Visualization of UMAP clustering results, reclassifying macrophages into two cell clusters, with different colors indicating different cell clusters; (D) Expression status of marker genes in each cell cluster; (E) Classification of macrophages into Macrophage_1 and Macrophage_2 cells based on marker genes; (F) UMAP clustering results showing the cell distribution of Macrophage_1 and Macrophage_2, with different colors indicating different subtypes of macrophages; (G) Heatmap of the top 10 genes expressed in Macrophage_1 and Macrophage_2; (H) Expression patterns of selected cell-specific marker genes in different cell subtypes, with darker blue indicating higher average expression levels and larger circles representing more cells expressing the gene; (I) Expression distribution of marker genes for different macrophage subtypes; (J) Proportions of Macrophage_1 and Macrophage_2 cells in each sample; (K) Bar chart comparing the cell numbers of different macrophage subtypes, with red representing Control group (n=28) and blue representing HF group (n=17); (L) Box plot showing the changes in proportions of macrophage subtypes, with red representing Control group (n=28) and blue representing HF group (n=17), * indicates significance compared to Control group, ***p <0.001. Fig. S8. Analysis of Distribution and Expression Characteristics of T Cell Subsets. Note: (A) UMAP distribution of T cells in all samples, with different colors representing different samples; (B) Distribution of T cells in Control group (n=28) and HF group (n=17), with red representing Control group (n=28) and blue representing HF group (n=17); (C) Visualization of UMAP clustering results, reclassifying T cells into 4 cell clusters, with different colors indicating different cell clusters; (D) Expression status of marker genes in each cell cluster; (E) Classification of T cells into NKT (Natural killer T cells), CD8+_Effector_T cells, T_memory cells, and Proliferate_NKT cells based on marker genes; (F) UMAP clustering results showing the distribution of various T cell subsets, with different colors indicating different T cell subsets; (G) Heatmap of the top 10 genes expressed in each T cell subset; (H) Expression patterns of selected cell-specific marker genes in different cell subtypes, with darker blue indicating higher average expression levels and larger circles representing more cells expressing the gene; (I) Expression distribution of marker genes for different T cell subsets; (J) Proportions of each T cell subset in each sample; (K) Bar chart comparing the cell numbers of different T cell subsets, with red representing Control group (n=28) and blue representing HF group (n=17); (L) Box plot showing the changes in proportions of T cell subsets, with red representing Control group (n=28) and blue representing HF group (n=17).Fig. S9. Analysis of Age-Related AUCell in

CMs. Note: (A) Distribution of the number of genes detected in each single CM; (B) AUCell analysis results of age-related gene sets at the single-cell level in CMs, where the curve plot represents the activity distribution of the gene set, and the highlighted area (AUC) shows the concentration trend of gene activity regions; (C) UMAP visualization plot based on expression, with each cell colored according to its AUC score of the age-related gene set; (D) Violin plot showing the score differences of CM subtypes in aging; (E) Differences in AUC scores of CM subtypes based on age-related gene sets between HF group (n=17) and Control group (n=28), * indicates significance compared to Control group, ***p <0.001.Fig. S10. Analysis of Age-Related AUCell in Macrophages. Note: (A) Distribution of the number of genes detected in every single macrophage; (B) AUCell analysis results of age-related gene sets at the single-cell level in macrophages, where the curve plot represents the activity distribution of the gene set and the highlighted area shows the concentration trend of gene activity regions; (C) UMAP visualization plot based on expression, with each cell colored according to its AUC score of the age-related gene set; (D) Violin plot showing the score differences of macrophage subtypes in aging; (E) Differences in AUC scores of macrophage subtypes based on age-related gene sets between HF group (n=17) and Control group (n=28), * indicates significance compared to Control group, ***p <0.001.Fig. S11. Analysis of Age-Related AUCell in T Cell Subsets. Note: (A) Distribution of the number of genes detected in each single T cell; (B) AUCell analysis results of age-related gene sets at the single-cell level in T cell subsets, where the curve plot represents the activity distribution of the gene set, and the highlighted area (AUC) shows the concentration trend of gene activity regions; (C) UMAP visualization plot based on expression, with each cell colored according to its AUC score of the age-related gene set; (D) Violin plot showing the score differences of T cell subsets in aging; (E) Differences in AUC scores of T cell subsets based on age-related gene sets between HF group (n=17) and Control group (n=28), * indicates significance compared to Control group, **p <0.01, ***p <0.001. Fig. S12. Analysis of CMs Ferroptosis-Related AUCell Scores. Note: (A) Distribution of the number of genes detected in each single CM; (B) AUCell analysis results of the ferroptosis-related gene set at the single-cell level in CMs, where the curve represents the activity distribution of the gene set, and the highlighted area (AUC) indicates the concentrated trend of gene activity region; (C) UMAP visualization based on expression, with cells color-coded according to the AUC scores of the ferroptosis-related gene set; (D) Violin plot showing the score differences of CM subtypes in ferroptosis; (E) Differences in the AUCell scores based on the ferroptosis gene set in CM subtypes between the HF group (n=17) and the Control group (n=28), * indicates significant difference compared to the Control group, with ***p <0.001. Fig. S13. Analysis of Macrophages Ferroptosis-Related AUCell Scores. Note: (A) Distribution of the number of genes detected in each single macrophage; (B) AUCell analysis results of the ferroptosis-related gene set at the single-cell level in macrophages, where the curve represents the activity distribution of the gene set and the highlighted area (AUC) indicates the concentrated trend of gene activity region; (C) UMAP visualization based on expression, with cells color-coded according to the AUC scores of the ferroptosis-related gene set; (D) Violin plot showing the score differences of macrophage subtypes in ferroptosis; (E) Differences in the AUCell scores based on the ferroptosis gene set in macrophage subtypes between the HF group (n=17) and the Control group (n=28), * indicates significant difference compared to the Control group, with ***p <0.001. Fig. S14. Analysis of T Cell Ferroptosis-Related AUCell Scores. Note: (A) Distribution of the number of genes detected in each single T cell; (B) AUCell analysis results of the ferroptosis-related gene set at the single-cell level in T cells, where the curve represents the activity distribution of the gene set, and the highlighted area (AUC) indicates the concentrated trend of gene activity region; (C) UMAP visualization based on expression, with cells color-coded according to the AUC scores of the ferroptosis-related gene set; (D) Violin plot showing the score differences of T cell subsets in ferroptosis; (E) Differences in the AUCell scores based on the ferroptosis gene set in T cell subsets between the HF group (n=17) and the Control group (n=28), * indicates significant difference compared to the Control group, with ***p <0.001. Fig. S15. Analysis of CMs Inflammation-Related AUCell Scores. Note: (A) Distribution of the number of genes detected in each single CM; (B) AUCell analysis results of the inflammation-related gene set at the single-cell level in CMs, where the curve represents the activity distribution of the gene set, and the highlighted area (AUC) indicates the concentrated trend of gene activity region; (C) UMAP visualization based on expression, with cells color-coded according to the AUC scores of the inflammation-related gene set; (D) Violin plot showing the score differences of CM subtypes in inflammation; (E) Differences in the AUCell scores based on the inflammation gene set in CM subtypes between the HF group (n=17) and the Control group (n=28). Fig. S16. Analysis of Macrophages Inflammation-Related AUCell Scores. Note: (A) Distribution of the number of genes detected in each single macrophage; (B) AUCell analysis results of the inflammation-related gene set at the single-cell level in macrophages, where the curve represents the activity distribution of the gene set and the highlighted area (AUC) indicates the concentrated trend of gene activity region; (C) UMAP visualization based on expression, with cells color-coded according to the AUC scores of the inflammation-related gene set; (D) Violin plot showing the score differences of macrophage subtypes in inflammation; (E) Differences in the AUCell scores based on the inflammation gene set in macrophage subtypes between the HF group (n=17) and the Control group (n=28), * indicates significant difference compared to the Control group, with ***p <0.001. Fig. S17. Analysis of T Cell Inflammation-Related AUCell Scores. Note: (A) Distribution of the number of genes detected in each single T cell; (B) AUCell analysis results of the inflammation-related gene set at the single-cell level in T cells, where the curve represents the activity distribution of the gene set, and the highlighted area (AUC) indicates the concentrated trend of gene activity region; (C) UMAP visualization based on expression, with cells color-coded according to the AUC scores of the inflammation-related gene set; (D) Violin plot showing the score differences of T cell subsets in inflammation; (E) Differences in the AUCell scores based on the inflammation gene set in T cell subsets between the HF group (n=17) and the Control group (n=28), * indicates significant difference compared to the Control group, **p <0.01. Fig. S18. Differential Gene Enrichment Analysis in CM_1 Cells. Note: (A) Bubble diagram (left) and gene network diagram (right) of GO-BP enrichment analysis of 616 DEGs in CM_1 cells; (B) Bubble diagram (left) and gene network diagram (right) of GO-CC enrichment analysis of 616 DEGs in CM_1 cells; (C) Bubble diagram (left) and gene network diagram (right) of GO-MF enrichment analysis of 616 DEGs in CM_1 cells; (D) Bubble diagram (left) and gene network diagram (right) of KEGG enrichment analysis of 616 DEGs in CM_1 cells. In the bubble diagrams, the color of the circles represents the significance of enrichment, with colors ranging from blue to red indicating increasing significance, and the size of the circles represents the number of enriched genes. Fig. S19. Differential Gene Enrichment Analysis in CM_2 Cells. (A) Bubble diagram (left) and gene network diagram (right) of GO-BP enrichment analysis of 947 DEGs in CM_2 cells; (B) Bubble diagram (left) and gene network diagram (right) of GO-CC enrichment analysis of 947 DEGs in CM_2 cells; (C) Bubble diagram (left) and gene network diagram (right) of GO-MF enrichment analysis of 947 DEGs in CM_2 cells; (D) Bubble diagram (left) and gene network diagram (right) of KEGG enrichment analysis of 947 DEGs in CM_2 cells. In the bubble diagrams, the color of the circles represents the significance of enrichment, with colors ranging from blue to red indicating increasing significance, and the size of the circles represents the number of enriched genes. Fig. S20. Verification of lentivirus Transfection Efficiency. Note: (A) RT-qPCR to detect the change in STAT3 mRNA expression in CMs cells after silencing STAT3 with different sequences transfection; (B) Western blot to detect the change in STAT3 protein expression in CMs cells after silencing STAT3 with different sequences transfection; (C) RT-qPCR to detect the change in STAT3 mRNA expression in CMs cells after overexpressing STAT3 with different sequences transfection; (D) Western blot to detect the change in STAT3 protein expression in CMs cells after overexpressing STAT3 with different sequences transfection. Quantitative data are presented as Mean ± SD, with each cell experiment replicated 3 times, * indicates comparison between two groups, ****p <0.0001. Fig. S21. Results of Ultrasound Diagnostic

Instrument and Hemodynamic Measurements. (A-F) Statistical charts of parameters including IVSD, LVEDD, LVESD, LVPWD, LVEF, and fractional shortening detected by ultrasound diagnostic instrument in the heart tissues of each group of mice; (G-J) Statistical charts of parameters including LVEDP, LVSP, maximum rate of rise of left ventricular pressure (+dp/dt), and maximum rate of fall of left ventricular pressure (-dp/dt) detected by hemodynamic measurements in each group of mice; (K-L) Detection results of LVMI and RVMI in mice. Quantitative data are presented as Mean ± SD, with 6 mice in each group, * indicates comparison between two groups, *p <0.05, **p <0.01, ***p <0.001, ****p <0.0001. Fig. S22. In vivo toxicity evaluation after PN@Col administration. (A) HE staining to detect kidney and liver damage in mice, with 6 mice per experimental group (scale bar: 50 μm); (B) Cytokine detection using ELISA kits.

Acknowledgements
Not applicable.

Author contributions
Haoyuan Zheng and Yuan Tian contributed equally to the study. Haoyuan Zheng and Dongyu Li performed the majority of the experimental work, including in vitro and in vivo studies, data analysis, and interpretation. Yanxiao Liang supervised the study, designed the research framework, and provided critical feedback on the manuscript. Yuan Tian contributed to the laboratory experiments, particularly in the single-cell RNA sequencing and AUCell analysis. Yanxiao Liang wrote the manuscript with input from all authors. All authors read and approved the final manuscript.

Funding
Not applicable.

Data availability
The data underlying this article will be shared on reasonable request to the corresponding author.

Declarations

Ethics approval and consent to participate
All animal experiments were approved by the Animal Ethics Committee of Shengjing Hospital of China Medical University (No. 2024PS359K).

Consent for publication
Not applicable.

Competing interests
The authors declare no competing interests.

Author details
[1]Department of Cardiac Surgery, Shengjing Hospital of China Medical University, 36 Sanhao Street, Heping District, Shenyang 110004, China. [2]Department of Laboratory Medicine, Shengjing Hospital of China Medical University, Shenyang 110004, China.

Received: 7 November 2024 Accepted: 11 March 2025
Published online: 29 March 2025

References

1. Ricci Z, Romagnoli S, Ronco C. Cardiorenal syndrome. Crit Care Clin. 2021. https://doi.org/10.1016/j.ccc.2020.11.003.
2. Frantz S, Hundertmark MJ, Schulz-Menger J, Bengel FM, Bauersachs J. Left ventricular remodelling post-myocardial infarction: pathophysiology, imaging, and novel therapies. Eur Heart J. 2022. https://doi.org/10.1093/eurheartj/ehac223.
3. Yu T, Gao M, Sun G, Graffigna G, Liu S, Wang J. Cardiac rehabilitation engagement and associated factors among heart failure patients: a cross-sectional study. BMC Cardiovasc Disord. 2023. https://doi.org/10.1186/s12872-023-03470-x.
4. Casella M, Compagnucci P, et al. Recurrence of atrial fibrillation postablation: which is the most effective approach for detection? Minerva Cardiol Angiol Edizioni Minerva Medica. 2022. https://doi.org/10.3736/s2724-5683.22.05859-8.
5. Gong X, Zhang T, Feng S, Song D, Chen Y, Yao T, et al. Association between N-terminal pro-BNP and 12 months major adverse cardiac events among patients admitted with NSTEMI. Ann Palliat Med. 2021. https://doi.org/10.21037/apm-20-2538.
6. Tromp J, Ouwerkerk W, van Veldhuisen DJ, Hillege HL, Richards AM, van der Meer P, et al. A systematic review and network meta analysis of pharmacological treatment of heart failure with reduced ejection fraction. JACC Heart Failure. 2022. https://doi.org/10.1016/j.jchf.2021.09.004.
7. Banerjee D, Rosano G, Herzog CA. Management of heart failure patient with CKD Ovid. CJASN Technol. 2021. https://doi.org/10.2215/cjn.14180920.
8. Mwansa H, Lewsey S, Mazimba S, Breathett K. Racial/ethnic and gender disparities in heart failure with reduced ejection fraction. Curr Heart Fail Rep. 2025. https://doi.org/10.1007/s11897-021-00502-5.
9. Hong JA, Lee SE, Kim S, Kim M, Lee H, Cho H, et al. Determinants of left ventricular function improvement for cardiac resynchronization therapy candidates. ESC Heart Failure. 2021. https://doi.org/10.1002/ehf2.13765.
10. Sohns C, Fox H, Marrouche NF, Crijns HJGM, Costard-Jaeckle A, Bergau L, et al. Catheter ablation in end-stage heart failure with atrial fibrillation. N Engl J Med. 2023. https://doi.org/10.1056/nejmoa2306037.
11. Squires RW, Bonikowske AR. Cardiac rehabilitation for heart transplant patients: considerations for exercise training. Progress Cardiovasc Dis. 2022. https://doi.org/10.1016/j.pcad.2021.12.003.
12. Jankauskas SS, Kansakar U, Varzideh F, Wilson S, Mone P, Lombardi A, et al. Heart failure in diabetes. Metabolism. 2021. https://doi.org/10.1016/j.metabol.2021.154910.
13. Matsuura TR, Puchalska P, Crawford PA, Kelly DP. Ketones and the heart: metabolic principles and therapeutic implications. Circ Res. 2025. https://doi.org/10.1161/circresaha.123.321872.
14. Murphy MP, Bayir H, Belousov V, Chang CJ, Davies KJA, Davies MJ, et al. Guidelines for measuring reactive oxygen species and oxidative damage in cells and in vivo. Nat Metab. 2025. https://doi.org/10.1038/s42255-022-00591-z.
15. Batty M, Bennett MR, Yu E. The role of oxidative stress in atherosclerosis. Cells. 2022. https://doi.org/10.3390/cells11233843.
16. Chang C, Cheng H, Chou W, Huang Y, Hsieh P, Chu P, et al. Sesamin suppresses angiotensin-II-enhanced oxidative stress and hypertrophic markers in H9c2 cells. Environ Toxicol. 2023. https://doi.org/10.1002/tox.23853.
17. Akhigbe R, Ajayi A. The impact of reactive oxygen species in the development of cardiometabolic disorders: a review. Lipids Health Dis. 2021. https://doi.org/10.1186/s12944-021-01435-7.
18. Lei G, Zhuang L, Gan B. Targeting ferroptosis as a vulnerability in cancer. Nat Rev Cancer. 2025. https://doi.org/10.1038/s41568-022-00459-0.
19. Fang X, Ardehali H, Min J, Wang F. The molecular and metabolic landscape of iron and ferroptosis in cardiovascular disease. Nat Rev Cardiol. 2022. https://doi.org/10.1038/s41569-022-00735-4.
20. Wu X, Li Y, Zhang S, Zhou X. Ferroptosis as a novel therapeutic target for cardiovascular disease. Theranostics. 2021. https://doi.org/10.7150/thno.54113.
21. Winiarska-Mieczan A, Kwiecień M, Jachimowicz-Rogowska K, Donaldson J, Tomaszewska E, Baranowska-Wójcik E. Anti-inflammatory, antioxidant, and neuroprotective effects of polyphenols—polyphenols as an element of diet therapy in depressive disorders. IJMS. 2023. https://doi.org/10.3390/ijms24032258.
22. He H, Qin Q, Xu F, Chen Y, Rao S, Wang C, et al. Oral polyphenol-armored nanomedicine for targeted modulation of gut microbiota–brain interactions in colitis. Adv Sci. 2023. https://doi.org/10.1126/sciadv.adf3887.
23. Annaji M, Poudel I, Boddu SHS, Arnold RD, Tiwari AK, Babu RJ. Resveratrol-loaded nanomedicines for cancer applications. Cancer Rep. 2021. https://doi.org/10.1002/cnr2.1353.
24. Qiao L, Yang H, Gao S, Li L, Fu X, Wei Q. Research progress on self-assembled nanodrug delivery systems. J Mater Chem B Royal Soc Chem. 2022. https://doi.org/10.1039/d1tb02470a.

25. Guo J, Miao Y, Nie F, Gao F, Li H, Wang Y, et al. Zn-Shik-PEG nanoparticles alleviate inflammation and multi-organ damage in sepsis. J Nanobiotechnol. 2025. https://doi.org/10.1186/s12951-023-02224-3.
26. Grabska-Kobyłecka I, Szpakowski P, Król A, Książek-Winiarek D, Kobyłecki A, Głąbiński A, et al. Polyphenols and their impact on the prevention of neurodegenerative diseases and development. Nutrients. 2023. https://doi.org/10.3390/nu15153454.
27. Li H, Bi Q, Cui H, Lv C, Wang M. Suppression of autophagy through JAK2, STAT3 contributes to the therapeutic action of rhynchophylline on asthma. BMC Complement Med Ther. 2021. https://doi.org/10.1186/s12906-020-03187-w.
28. Wu L, Huang G, Hong H, Xu X, Lu X, Li J. MiR-452-5p facilitates retinoblastoma cell growth and invasion via the SOCS3, JAK2, STAT3 pathway. J Biochem & Molecular Tox. 2023. https://doi.org/10.1002/jbt.23501.
29. Zhuang L, Jia K, Chen C, Li Z, Zhao J, Hu J, et al. DYRK1B-STAT3 Drives cardiac hypertrophy and heart failure by impairing mitochondrial bioenergetics. Circulation. 2022. https://doi.org/10.1161/circulationaha.121.055727.
30. Sun J-Y, Du L-J, Shi X-R, Zhang Y-Y, Liu Y, Wang Y-L, et al. An IL-6, STAT3, MR, FGF21 axis mediates heart-liver cross-talk after myocardial infarction. Sci Adv Am Assoc Adv Sci. 2023. https://doi.org/10.1126/sciadv.ade4110.
31. Huang F, Zhang S, Li X, Huang Y, He S, Luo L. STAT3-mediated ferroptosis is involved in ulcerative colitis. Free Radical Biol Med. 2022. https://doi.org/10.1016/j.freeradbiomed.2022.06.242.
32. Zhang W, Gong M, Zhang W, Mo J, Zhang S, Zhu Z, et al. Thiostrepton induces ferroptosis in pancreatic cancer cells through STAT3, GPX4 signalling. Cell Death Dis. 2022. https://doi.org/10.1038/s41419-022-05082-3.
33. Zhu M, Peng L, Huo S, Peng D, Gou J, Shi W, et al. STAT3 signaling promotes cardiac injury by upregulating NCOA4-mediated ferritinophagy and ferroptosis in high-fat-diet fed mice. Free Radical Biol Med. 2023. https://doi.org/10.1016/j.freeradbiomed.2023.03.003.
34. Bock FJ, Tait SWG. Mitochondria as multifaceted regulators of cell death. Nat Rev Mol Cell Biol. 2025. https://doi.org/10.1038/s41580-019-0173-8.
35. Gao M, Yi J, Zhu J, Minikes AM, Monian P, Thompson CB, et al. Role of mitochondria in ferroptosis. Molecular Cell. 2019. https://doi.org/10.1016/j.molcel.2018.10.042.
36. Chiba T, Yamada M, Hashimoto Y, Sato M, Sasabe J, Kita Y, et al. Development of a femtomolar-acting humanin derivative named colivelin by attaching activity-dependent neurotrophic factor to its n terminus: characterization of colivelin-mediated neuroprotection against Alzheimer's disease-relevant insultsin vitroandin vivo. J Neurosci. 2005. https://doi.org/10.1523/jneurosci.3348-05.2005.
37. Zhao H, Feng Y, Wei C, Li Y, Ma H, Wang X, et al. Colivelin rescues ischemic neuron and axons involving JAK/STAT3 signaling pathway. Neuroscience. 2019. https://doi.org/10.1016/j.neuroscience.2019.07.020.
38. Li P, Li J-L, Feng X-H, Li Z-P, Yin F, Yan J, et al. Comparison of changes in left ventricular gene expression profiles from different cardiac hypertrophy models in rats. Sheng Li Xue Bao China. 2004;56:210–8.
39. Nobata S, Ventura A, Kaiya H, Takei Y. 2010. Diversified cardiovascular actions of six homologous natriuretic peptides (ANP, BNP, VNP, CNP1, CNP3, and CNP4) in conscious eels American Journal of Physiology Regulatory, Integrative and Comparative Physiology. American Physiological Society. https://doi.org/10.1152/ajpregu.00789.2009
40. Olsen MB, Gregersen I, Sandanger Ø, Yang K, Sokolova M, Halvorsen BE, et al. Targeting the inflammasome in cardiovascular disease. JACC Basic Trans Sci. 2022. https://doi.org/10.1016/j.jacbts.2021.08.006.
41. Griffin JM, Rosenthal JL, Grodin JL, Maurer MS, Grogan M, Cheng RK. ATTR amyloidosis current and emerging management strategies. JACC CardioOncol. 2021. https://doi.org/10.1016/j.jaccao.2021.06.006.
42. Sun L, Wang H, Yu S, Zhang L, Jiang J, Zhou Q. Herceptin induces ferroptosis and mitochondrial dysfunction in H9c2 cells. Int J Mol Med Spandidos Publ. 2021. https://doi.org/10.3892/ijmm.2021.5072.
43. Yin P, Wu Y, Long X, Zhu S, Chen S, Lu F, et al. HACE1 expression in heart failure patients might promote mitochondrial oxidative stress and ferroptosis by targeting NRF2. Aging Impact J. 2025. https://doi.org/10.1632/aging.205272.
44. van der Pol A, van Gilst WH, Voors AA, van der Meer P. Treating oxidative stress in heart failure: past, present and future. Eur J Heart Fail. 2018. https://doi.org/10.1002/ejhf.1320.
45. Wang X, Zhang G, Dasgupta S, Niewold EL, Li C, Li Q, et al. ATF4 protects the heart from failure by antagonizing oxidative stress. Circ Res. 2022. https://doi.org/10.1161/circresaha.122.321050.
46. Chen J, Xu F, Ruan X, Sun J, Zhang Y, Zhang H, et al. Therapeutic targets for inflammatory bowel disease: proteome-wide Mendelian randomization and colocalization analyses. eBioMedicine. 2023. https://doi.org/10.1016/j.ebiom.2023.104494.
47. Dong S, Guo X, Han F, He Z, Wang Y. Emerging role of natural products in cancer immunotherapy. Acta Pharmaceutica Sinica B. 2025. https://doi.org/10.1016/j.apsb.2021.08.020.
48. Foerster EG, Mukherjee T, Cabral-Fernandes L, Rocha JDB, Girardin SE, Philpott DJ. How autophagy controls the intestinal epithelial barrier. Autophagy. 2021. https://doi.org/10.1080/15548627.2021.1909406.
49. Han R, Lan X, Han Z, Ren H, Aafreen S, Wang W, et al. Improving outcomes in intracerebral hemorrhage through microglia/macrophage-targeted IL-10 delivery with phosphatidylserine liposomes. Biomaterials. 2023. https://doi.org/10.1016/j.biomaterials.2023.122277.
50. Zhu Y, Wang A, Zhang S, Kim J, Xia J, Zhang F, et al. Paclitaxel-loaded ginsenoside Rg3 liposomes for drug-resistant cancer therapy by dual targeting of the tumor microenvironment and cancer cells. J Adv Res. 2023. https://doi.org/10.1016/j.jare.2022.09.007.
51. Feng Q, Xiao K. Nanoparticle-mediated delivery of STAT3 inhibitors in the treatment of lung cancer. Pharmaceutics. 2022. https://doi.org/10.3390/pharmaceutics14122787.
52. Soames RW, Evans AA. Female gait patterns: the influence of footwear. Ergonomics. 2025. https://doi.org/10.1080/00140138708969785.
53. Cheng P, Wang X, Liu Q, Yang T, Dai E, Sha W, et al. LuQi formula attenuates cardiomyocyte ferroptosis via activating Nrf2/GPX4 signaling axis in heart failure. Phytomedicine. 2024. https://doi.org/10.1016/j.phymed.2024.155357.
54. Haghikia A, Missol-Kolka E, Tsikas D, Venturini L, Brundiers S, Castoldi M, et al. Signal transducer and activator of transcription 3-mediated regulation of miR-199a-5p links cardiomyocyte and endothelial cell function in the heart: a key role for ubiquitin-conjugating enzymes. Eur Heart J. 2010. https://doi.org/10.1093/eurheartj/ehq369.
55. Ren K, Li B, Jiang L, Liu Z, Wu F, Zhang Y, et al. circ_0023461 silencing protects cardiomyocytes from hypoxia-induced dysfunction through targeting miR-370-3p, PDE4D signaling. Oxidative Med Cellular Longevity. 2021. https://doi.org/10.1155/2021/8379962.
56. Amoozgar Z, Park J, Lin Q, Yeo Y. Low molecular-weight chitosan as a pH-sensitive stealth coating for tumor-specific. Drug Delivery Mol Pharm Am Chem Soc (ACS). 2012. https://doi.org/10.1021/mp2005615.
57. Shirakabe A, Zhai P, Ikeda Y, Saito T, Maejima Y, Hsu C-P, et al. Drp1-dependent mitochondrial autophagy plays a protective role against pressure overload-induced mitochondrial dysfunction and heart failure. Circulation. 2016. https://doi.org/10.1161/circulationaha.115.020502.
58. Huang C-Y, Pai P-Y, Kuo C-H, Ho T-J, Lin J-Y, Lin D-Y, et al. p53-mediated miR-18 repression activates HSF2 for IGF-IIR-dependent myocyte hypertrophy in hypertension-induced heart failure. Cell Death Dis. 2017. https://doi.org/10.1038/cddis.2017.320.
59. Garrott K, Dyavanapalli J, Cauley E, Dwyer MK, Kuzmiak-Glancy S, Wang X, et al. Chronic activation of hypothalamic oxytocin neurons improves cardiac function during left ventricular hypertrophy-induced heart failure. Cardiovasc Res. 2025. https://doi.org/10.1093/cvr/cvx084.
60. Feng X, Hou Y, Liu J, Yan F, Dai M, Chen M, et al. A multi-targeting immunotherapy ameliorates multiple facets of Alzheimer's disease in 3xTg mice. Npj Vaccines. 2024. https://doi.org/10.1038/s41541-024-00942-9.

Publisher's Note